2. Birkeland Currents in Cosmic Plasma

2.1 History of Birkeland Currents

An electromotive force $\phi = \int \mathbf{v} \times \mathbf{B} \cdot d\mathbf{l}$ giving rise to electrical currents in conducting media is produced wherever a relative perpendicular motion of plasma and magnetic field lines exist (Section 3.5.2). An example of this is the sunward convective motion of the magnetospheric plasma that cuts the earth's dipole field lines through the equatorial plane, thereby producing a Lorentz force that drives currents within the auroral circuit. The tendency for charged particles to follow magnetic lines of force and therefore produce field-aligned currents has resulted in the widespread use of the term "Birkeland Currents" in space plasma physics. Their discovery in the earth's magnetosphere in 1974 has resulted in a drastic change of our understanding of aurora dynamics, now attributed to the filamentation of Birkeland charged-particle sheets following the earth's dipole magnetic field lines into vortex current bundles. In anticipation of the importance of Birkeland currents in astrophysical settings, Fälthammar (1986) states: "A reason why Birkeland currents are particularly interesting is that, in the plasma forced to carry them, they cause a number of plasma physical processes to occur (waves, instabilities, fine structure formation). These in turn lead to consequences such as acceleration of charged particles, both positive and negative, and element separation (such as preferential ejection of oxygen ions). Both of these classes of phenomena should have a general astrophysical interest far beyond that of understanding the space environment of our own Earth."

Birkeland currents have a long and colorful history. Inspired by his famous terrella experiments at the beginning of the twentieth century (Figure 2.1) and by his extensive studies of geomagnetic data recorded during magnetic storms, the Norwegian scientist Kristian Birkeland (1867-1917) suggested that the aurora was associated with electric "corpuscular rays" emanating from the sun and deflected to the polar regions of the earth by the geomagnetic field. Birkeland recognized that the magnetic disturbances recorded on the earth's surface below the auroral region were due to intense currents flowing horizontally above. He suggested that these currents, now called "auroral electrojet" currents, were coupled to vertical currents that flowed along geomagnetic field lines into and away from the lower ionosphere. The system of field-aligned currents suggested by Birkeland is shown in Figure 2.2a.

The existence of magnetic field-aligned "Birkeland" currents was disputed because it is not possible to distinguish unambiguously between current systems that are field-aligned and those that are completely ionospheric from a study of surface magnetic field measurements. Sydney Chapman, the noted British geophysicist, developed mathematically elegant models of currents that were contained completely within the earth's ionosphere that could adequately account for

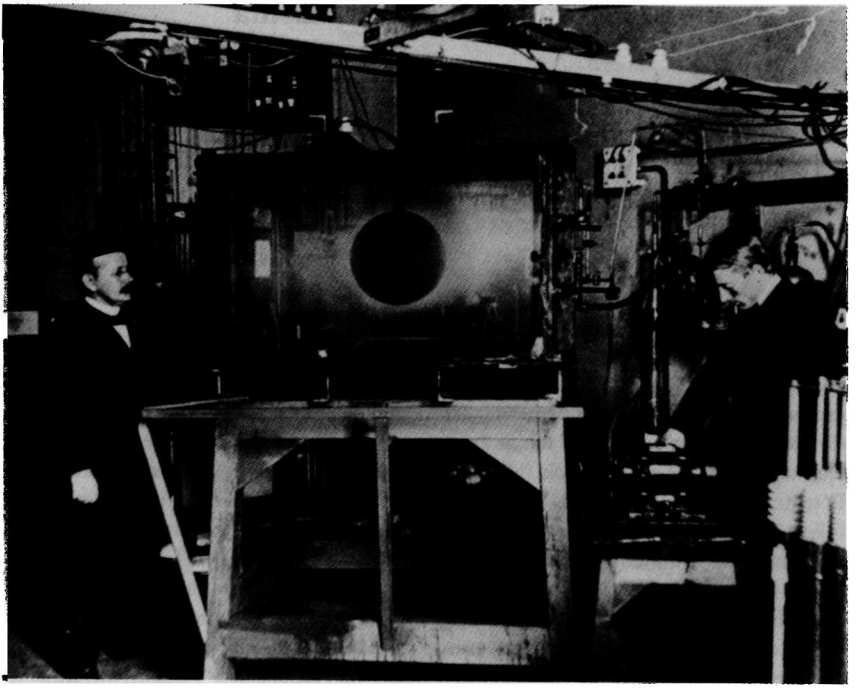

Figure 2.1. Birkeland (left), the founder of experimental astrophysics, is shown here with his assistant, K. Devik, and his "terrella," a magnetized globe representing the earth.

ground-based magnetic field observations obtained during magnetic storms. Figure 2.2b shows the "atmospheric current system" developed by Chapman in 1927.

Hannes Alfvén, the Swedish engineer and physicist, advocated the idea of Birkeland currents and developed a theory for the generation of these currents by the solar wind [Alfvén 1939]. Figure 2.2c shows Alfvén's diagram for these currents.

The first satellite measurements of Birkeland currents were provided by Zmuda et al. (1966, 1967) with a single axis magnetometer on board the navigation satellite 1963-38C at an altitude of ~1100 km. The magnetic disturbances observed were initially interpreted as hydromagnetic waves, but it was soon realized that their latitudinal extent was not appropriate for waves and they were interpreted as being due to Birkeland currents [Cummings and Dessler 1967]. Today, Birkeland currents are routinely measured by a variety of rocket and satellite instruments.

The location, flow direction, and intensity of Birkeland currents have been studied by several satellites, and a statistical map is provided in Figure 2.3. This distribution, plotted on an invariant (magnetic) latitude and geomagnetic local time polar dial, was determined from hundreds of orbits of the TRIAD satellite over the polar regions [Iijima and Potemra 1976]. It shows that there are well defined patterns of these currents, and these patterns coincide approximately with the auroral

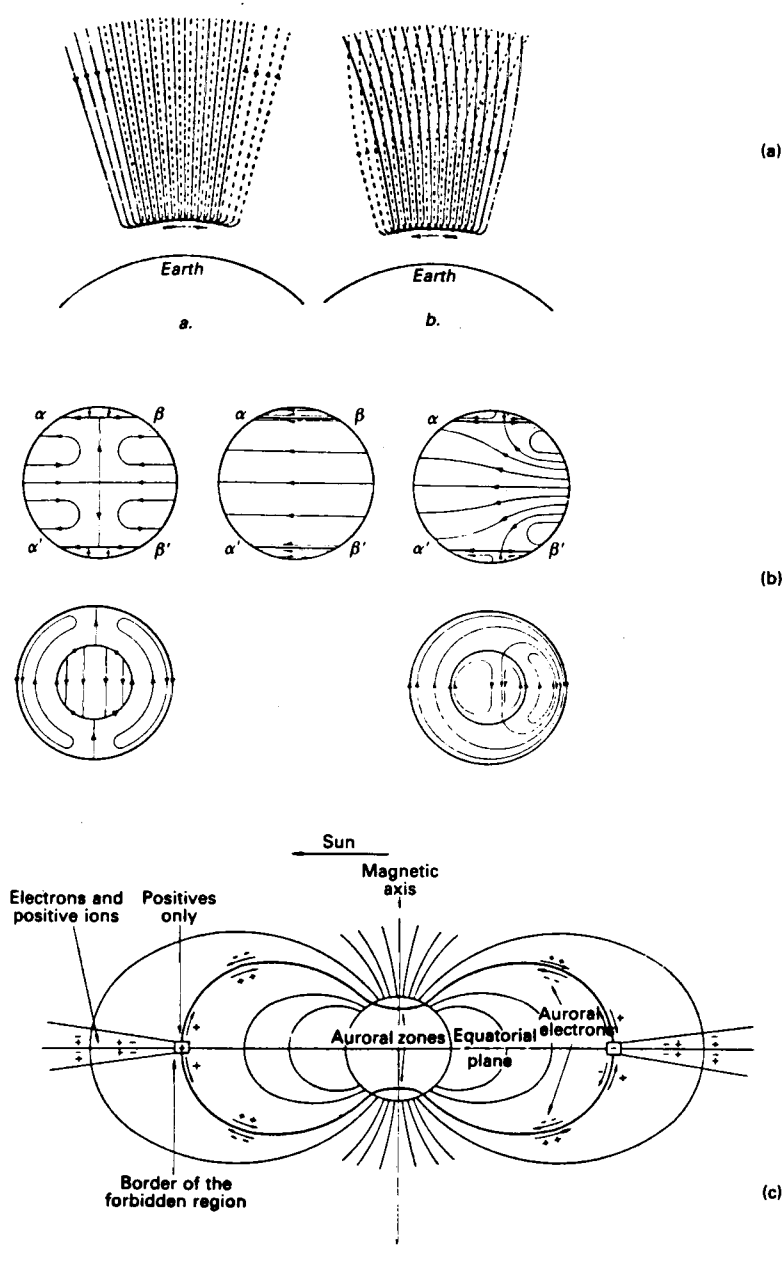

Figure 2.2. Historical diagrams of auroral current systems from: **(a)** Birkeland (1908), **(b)** Chapman (1927), **(c)** Alfvén (1939).

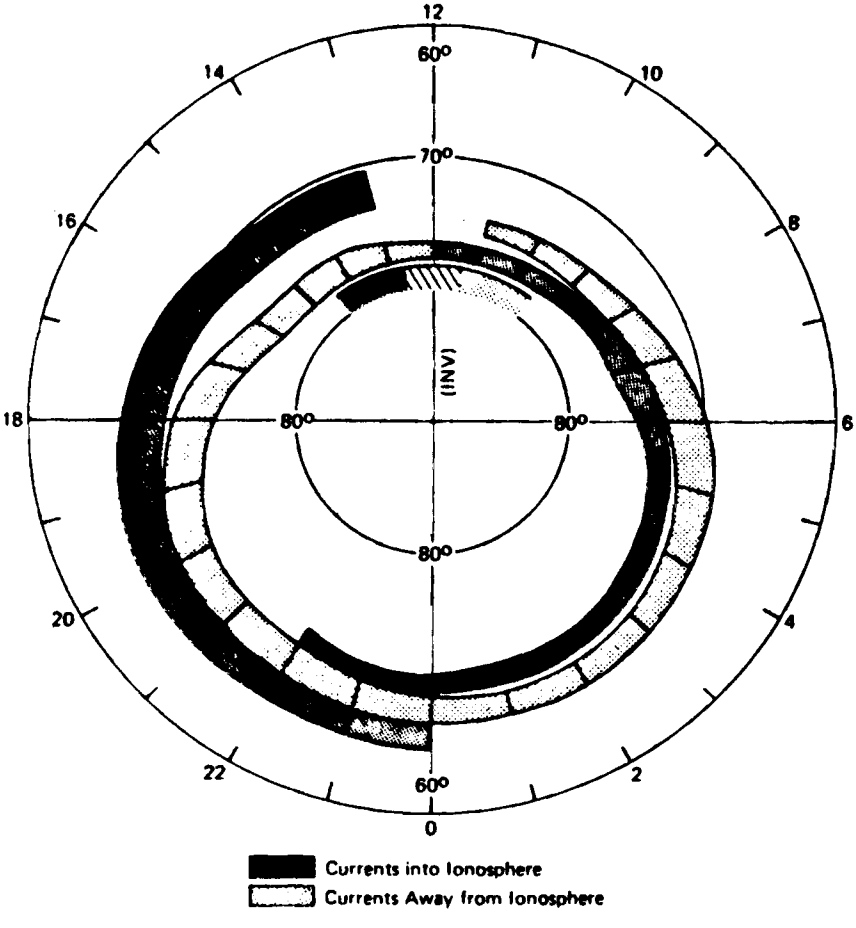

Figure 2.3. Distribution of Birkeland currents at earth's north pole as determined by TRIAD satellite magnetic field observations. The dark areas denote currents into the ionosphere while the shaded areas denote currents away from the ionosphere. The hatched area near noon indicates confused current directions (courtesy T. Potemra).

zone. The inflowing currents are at latitude 70° and the outflowing currents are at 74°–78° from about noon to midnight, then reverse directions from midnight to noon.

The magnitude and flow direction of Birkeland currents are determined from the magnetic field observations with Maxwell's equation Eq.(1.2), $\mathbf{j} = (1/\mu_0)\nabla \times \Delta \mathbf{B}$ (where $\Delta \mathbf{B}$ is the magnetic perturbation). For currents flowing parallel to the geomagnetic field and in sheets aligned in the east–west direction (with infinite extent), this vector formula reduces to the scalar gradient, $j_z = 1/\mu_0 \partial(\Delta B_y)/\partial x$ where j_z is the current flowing along the main geomagnetic field

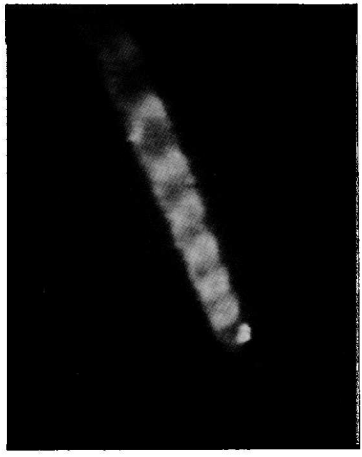

Figure 2.4. A glowing beam of electrons spirals upwards along the earth's magnetic field. This television image was taken during the Echo 7 sounding-rocket experiment. The view shows a portion of the corkscrew beam several hundred meters long from top to bottom and 17 meters across. The small, bright glow at the lower end of the beams is the accelerator that produced the energetic particles (courtesy John R. Winckler, University of Minnesota).

(in the z direction), ΔB_y is the perturbation in the eastward (y) direction, and x is the northward direction.

Birkeland currents not only heat the upper atmosphere, increasing the drag on low altitude earth circling satellites, but cause substantial density depletions. Electric fields along the dipole magnetic field lines can give rise to field-aligned currents that reduce the ionospheric topside electron and ion densities [Block and Fälthammar 1969]. In the topside there is then an excess of ionization in contrast to low altitudes where recombination dominates. The net effect is an upward flux of neutral particles that are ionized at high altitudes. Auroral primary particles are charged particles with the proper sign that have been accelerated downward. Closure of the global circuit is accomplished by particles with the opposite sign, that move out of the magnetosphere and precipitate in another region of the ionosphere with reversed polarity. Current measurements suggest that the supply of plasma from the solar wind is negligible in relation to the supply of plasma from the closed loop ionospheric/magnetospheric system.

As an example of a manmade "Birkeland current," a charged-particle beam in space undergoing a helical motion along the Earth's magnetic field is shown in Figure 2.4. The physics of this beam behavior are examined in Sections 2.5.3 and 2.9.7.

2.2 Field-Aligned Currents in Laboratory Plasma

In the laboratory, filamentary and helical structure is a common morphology exhibited by energetic plasmas. X ray pinhole photographs, optical streak and framing camera photographs, and

laser holograms often show a filamentary, magnetic "rope-like" structure from plasmas produced in multi-terawatt pulse power generators or in dense plasma focus machines (Figure 1.2). Often, the cross-sectional patterns from filamentation in hollow electron beams are recorded onto observing screens or witness plates. Regardless of size or current, the patterns are those of vortices (Figures 1.20–1.21). In the dense plasma focus the vortices have dimensions of a few microns while in laboratory electron beams the vortices may be a few centimeters in diameter. This size variation of 4 orders of magnitude is extended to nearly 9 orders of magnitude when auroral vortex recordings are directly compared to the laboratory data. With regard to actual current magnitudes; filamentation occurs over nearly 12 orders of magnitude while coarser resolution experiments show that the phenomena probably transcends at least 14 orders of magnitude, from microampere to multi-megaampere electron beams.

2.3 Field-Aligned Currents in Astrophysical Plasmas

As far as we know, most cosmic low density plasmas also depict a filamentary structure. For example, filamentary structures are found in the following cosmic plasmas, all of which are observed or are likely to be associated with electric currents:

(1) In the aurora, filaments parallel to the magnetic field are often observed. These can sometimes have dimensions down to about 100 m (Figure 1.21).

(2) Inverted V events and the in-situ measurements of strong electric fields in the magnetosphere (10^5–10^6 A, 10^8 m) demonstrate the existence of filamentary structures.

(3) In the ionosphere of Venus, "flux ropes", whose filamentary diameters are typically 20 km, are observed.

(4) In the sun, prominences (10^{11} A), spicules, coronal streamers, polar plumes, etc., show filamentary structure whose dimensions are of the order 10^7–10^8 m (Figure 1.10).

(5) Cometary tails often have a pronounced filamentary structure (Figure 1.8).

(6) In the interstellar medium and in interstellar clouds there is an abundance of filamentary structures [e.g., the Veil nebula (Figure 1.13), the Lagoon nebula, the Orion nebula, and the Crab nebula].

(7) The center of the Galaxy, where twisting plasma filaments, apparently held together by a magnetic field possessing both azimuthal and poloidal components, extend for nearly 60 pc (10^{18}m) (Figure 1.14).

(8) Within the radio bright lobes of double radio galaxies, where filament lengths may exceed 20 kpc (6×10^{20}m) (Figure 1.15).

Regardless of scale, the motion of charged particles produces a self-magnetic field that can act on other collections of particles or plasmas, internally or externally. *Plasmas in relative motion are coupled via currents that they drive through each other.* Currents are therefore expected in a universe of inhomogeneous astrophysical plasmas of all sizes.

2.4 Basic Equations of Magnetohydrodynamics

2.4.1 General Plasma Fluid Equations

Fundamental equations for the plasma velocity, magnetic field, plasma density, electric current, plasma pressure, and plasma temperature can be derived from macroscopic averages of currents, fields, charge densities, and mass densities. In this "fluid" treatment, the Maxwell–Hertz–Heaviside equations (1.1)-(1.4) are coupled to the moments of the Boltzmann equation for a highly ionized plasma.

The evolution of the distribution function $f(\mathbf{r},\mathbf{p},t)$ for particles with charge q and mass m is described by the Boltzmann equation

$$\left[\frac{\partial}{\partial t}+\mathbf{v}\cdot\frac{\partial}{\partial \mathbf{r}}+q\left(\mathbf{E}+\mathbf{v}\times\mathbf{B}\right)\cdot\frac{\partial}{\partial \mathbf{p}}\right]f(\mathbf{r},\mathbf{p},t)=\left(\frac{\partial f}{\partial t}\right)_{collisions} \tag{2.1}$$

which is an expression of Liouville's theorem for the incompressible motion of particles in the six-dimensional phase space $(\mathbf{r}, \mathbf{p}, t)$.

In the fluid description the particle density $n\ (\mathbf{r},t)$, mean velocity $\overline{\mathbf{v}}\ (\mathbf{r},t)$, momentum $\overline{\mathbf{p}}\ (\mathbf{r},t)$, pressure $\mathbf{P}\ (\mathbf{r},t)$, and friction $\mathbf{R}\ (\mathbf{r},t)$ are defined by

$$n\ (\mathbf{r},t)\equiv\int d^3p\, f(\mathbf{r},\mathbf{p},t) \tag{2.2}$$

$$n\ (\mathbf{r},t)\ \overline{\mathbf{v}}\ (\mathbf{r},t)\equiv\int d^3p\ \ \mathbf{v}f(\mathbf{r},\mathbf{p},t) \tag{2.3}$$

$$n\ (\mathbf{r},t)\ \overline{\mathbf{p}}\ (\mathbf{r},t)\equiv\int d^3p\ \ \mathbf{p}f(\mathbf{r},\mathbf{p},t) \tag{2.4}$$

$$\mathbf{P}\ (\mathbf{r},t)\equiv\int d^3p\ \ [\overline{\mathbf{p}}-\mathbf{p}\ (\mathbf{r},t)][\overline{\mathbf{v}}-\mathbf{v}\ (\mathbf{r},t)]f(\mathbf{r},\mathbf{p},t) \tag{2.5}$$

$$\mathbf{R}\ (\mathbf{r},t)\equiv\int d^3p\ \ [\mathbf{p}-\overline{\mathbf{p}}]\left(\frac{\partial f}{\partial t}\right)_{collisions} \tag{2.6}$$

where the momentum $\mathbf{p}$ and velocity $\mathbf{v}$ are related by

$$\mathbf{p}=m\gamma\mathbf{v} \tag{2.7}$$

The fields $\mathbf{E}(\mathbf{r},t)$ and $\mathbf{B}\ (\mathbf{r},t)$ in Eq.(2.1) are self-consistently solved from Eqs.(1.1)–(1.4) with

$$\rho\ (\mathbf{r},t)\equiv e\int d^3p\, f(\mathbf{r},\mathbf{p},t) \tag{2.8}$$

$$\mathbf{j}\ (\mathbf{r},t)\equiv e\int d^3p\ \ \mathbf{v}f(\mathbf{r},\mathbf{p},t) \tag{2.9}$$

Taking the moments $\int d^3 p$ and $\int d^3 p \ \mathbf{p}$ of the Boltzmann equation yields the two-fluid equations [Rose and Clark 1961, Thompson 1962, Alfvén and Carlqvist 1963, Chen 1984] for ions and electrons $\alpha = i, e$,

$$\frac{\partial n_\alpha}{\partial t} + \nabla \cdot (n_\alpha \mathbf{v}_\alpha) = 0 \tag{2.10}$$

$$n_\alpha \frac{d\mathbf{p}_\alpha}{dt} = q_\alpha n_\alpha (\mathbf{E} + \mathbf{v}_\alpha \times \mathbf{B}) - \nabla \cdot \mathbf{P}_\alpha + \mathbf{R}_\alpha - n_\alpha m_\alpha \nabla \phi_G \tag{2.11}$$

These are called the continuity and momentum equations, respectively. The continuity equation, as written, is valid if ionization and recombination are not important.

Conservation of linear momentum dictates that

$$\mathbf{R}_i + \mathbf{R}_e = 0 \tag{2.12}$$

The two fluid equations are the moments, or averages, of the kinetic plasma description and no longer contain the discrete particle phenomena such as double layers from charge separation and synchrotron radiation. Nevertheless, this approach is useful in studying bulk plasma flow and behavior.

A single fluid hydromagnetic force equation may be obtained by substituting $\alpha = i, e$ into Eq.(2.11) and adding to get,

$$\rho_m \frac{\partial \mathbf{v}_m}{\partial t} = \rho \, \mathbf{E} + \mathbf{j} \times \mathbf{B} - \nabla p - \rho_m \nabla \varphi_G \tag{2.13}$$

which relates the forces to mass and acceleration for the following averaged quantitites:

$\rho_m = n_e m_e + n_i m_i$	mass density	
$\mathbf{j_m} = n_e m_e \bar{\mathbf{v}}_e + n_i m_i \bar{\mathbf{v}}_i$	mass current	
$\mathbf{v_m} = \mathbf{j_m} / \rho_m$	averaged velocity	(2.14)
$\rho = n_e q_e + n_i q_i$	charge density	
$\mathbf{j} = n_e q_e \bar{\mathbf{v}}_e + n_i q_i \bar{\mathbf{v}}_i$	current density	

The first term in Eq.(2.14) is caused by the electric field, the second term derives from the motion of the current flow across the magnetic field, the third term is due to the pressure gradient [Eq.(2.14) is valid for an isotropic distribution $\nabla \cdot \mathbf{P} \rightarrow \nabla p$ where $p \equiv nkT$], and the fourth term is due to the gravitational potential φ_G. The near absence of excess charge $\rho = e(n_i - n_e) \approx 0$, for $q_{i,e} = \pm e$, is a characteristic of the plasma state; however, this does not mean that electrostatic fields [e.g., those deriving from Eq.(1.3)] are unimportant.[1]

Completing the single fluid description is the equation for mass conservation,

$$\frac{\partial \rho_m}{\partial t} + \nabla \cdot (\rho_m \mathbf{v}_m) = 0 \tag{2.15}$$

In addition to Eqs.(2.13) and (2.15), we find it useful to add the equation for magnetic induction,

$$\frac{\partial \mathbf{B}}{\partial t} = \nabla \times (\mathbf{v}_m \times \mathbf{B}) + \frac{1}{\mu \sigma} \nabla^2 \mathbf{B} \tag{2.16}$$

obtained by taking the curl of Ohm's law

$$\mathbf{j} = \sigma(\mathbf{E} + \mathbf{v} \times \mathbf{B})$$

where σ is the electrical conductivity (Table 1.6).

2.4.2 Magnetic Reynolds and Lundquist Numbers

The significance of Eq.(2.16) in which $(\mu \sigma)^{-1}$ is the *magnetic diffusivity*, is that changes in the magnetic field strength are caused by the transport of the magnetic field with the plasma (as represented by the first term on the right-hand-side), together with diffusion of the magnetic field through the plasma (second term on the right-hand-side). In order of magnitude, the ratio of the first to the second term is the *magnetic Reynolds number*

$$R_m = \mu \sigma V_c l_c \tag{2.17}$$

in terms of a characteristic plasma speed V_c and a characteristic scale length l_c. A related quantity is the *Lundquist parameter*

$$L_u = \mu \sigma V_A l_c \tag{2.18}$$

where

$$V_A = \frac{B}{\sqrt{\mu \rho_m}} \tag{2.19}$$

is the Alfvén speed. It may be written as the ratio

$$L_u = \frac{\tau_d}{\tau_A} \tag{2.20}$$

of the *magnetic diffusion time*

$$\tau_d = \mu \sigma l_c^2 \tag{2.21}$$

to the *Alfvén travel time*

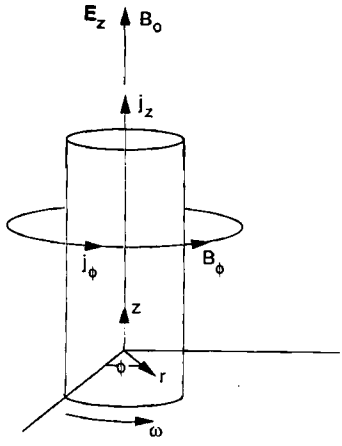

Figure 2.5. A current-carrying plasma pinch undergoing rotation at angular frequency ω.

$$\tau_A = l_c/V_A \tag{2.22}$$

2.5 The Generalized Bennett Relation

A generalized Bennett relation follows directly from Eq.(2.13) and Eqs.(1.1)-(1.4). Consider a current-carrying, magnetic-field-aligned cylindrical plasma of radius a which consists of electrons, ions, and neutral gas having the densities n_e, n_i, and n_n, and the temperatures T_e, T_i, and T_n, respectively. A current of density $\mathbf{j}_z$ flows in the plasma along the axis of the cylinder which coincides with the z–axis. As a result of the axial current a toroidal magnetic field $\mathbf{B}_\varphi$ is induced (Figure 2.5). An axial electric field is also present. Thus, there exists the electric and magnetic fields

$$\mathbf{E} = (E_r, E_\phi, E_z)$$

$$\mathbf{B} = (0, B_\phi, B_z)$$

The derivation of the generalized Bennett relation for this plasma is straightforward, but lengthy [Witalis 1981], and the final result is

$$\frac{1}{4}\frac{\partial^2 J_0}{\partial t^2} = W_{\perp kin} + \Delta W_{Ez} + \Delta W_{Bz} + \Delta W_k$$
$$-\frac{\mu_0}{8\pi} I^2(a) - \frac{1}{2} G \overline{m}^2 N^2(a) + \frac{1}{2}\pi a^2 \varepsilon_0 \left(E_r^2(a) - E_\phi^2(a)\right) \tag{2.23}$$

where

$$J_0 = \int_0^{2\pi}\int r^2 \rho_m \, r \, dr \, d\phi = \int_0^a r^2 \rho_m \, 2\pi r \, dr \tag{2.24}$$

is the total moment of inertia with respect to the z axis. (As the mass m of a particle or beam is its resistance to linear acceleration, J_0 is the beam resistance to angular displacement or rotation). The quantities ΔW are defined by

$$\Delta W_{Ez} \equiv W_{Ez} - \frac{1}{2}\varepsilon_0 E_z^2(a)\,\pi a^2 \tag{2.25}$$

$$\Delta W_{Bz} \equiv W_{Bz} - \frac{1}{2\mu_0} B_z^2(a)\,\pi a^2 \tag{2.26}$$

$$\Delta W_k \equiv W_k - p(a)\,\pi a^2 \tag{2.27}$$

where $E_z(a)$, $B_z(a)$, and $p(a)$ denote values at the boundary $r = a$. The individual energies W are defined as follows:

$$W_{\perp kin} = \frac{1}{2}\int_0^a \rho_m(r)\left[v_\phi^2(r) + v_r^2(r)\right] 2\pi r \, dr \tag{2.28}$$

which is the kinetic energy per unit length due to beam motion transverse to the beam axis,

$$W_{Bz} = \frac{1}{2\mu_0}\int_0^a B_z^2(r)\, 2\pi r \, dr \qquad \text{self-consistent } B_z \text{ energy per unit length;} \tag{2.29}$$

$$W_{Ez} = \frac{\varepsilon_0}{2}\int_0^a E_z^2(r)\, 2\pi r \, dr \qquad \text{self-consistent } E_z \text{ energy per unit length;} \tag{2.30}$$

$$W_k = \int_0^a p\, 2\pi r dr \qquad \text{thermokinetic energy per unit length;} \qquad (2.31)$$

$$I(a) = \int_0^a j_z\, 2\pi r dr \qquad \text{axial current inside the radius } a\text{;} \qquad (2.32)$$

$$N(a) = \int_0^a n\, 2\pi r dr \qquad \text{total number of particles per unit length;} \qquad (2.33)$$

where $n = n_i + n_e + n_n$ is the total density of ions, electrons, and neutral particles. The mean particle mass is $\overline{m} = (n_i m_i + n_e m_e + n_n m_n)/n$.

The self-consistent electric field can be determined from Eq.(1.13)

$$r^{-1}\frac{d(rE_r)}{dr} = -\frac{e}{\varepsilon_0}(n_e - n_i)$$

and is given by

$$E_r(r) = \frac{-en_e(1-f_e)}{2\varepsilon_0} r \qquad 0 \le r \le a$$

$$= \frac{-en_e(1-f_e)}{2\varepsilon_0}\frac{a^2}{r} \qquad r \ge a$$

Neglecting the displacement current, the self-consistent magnetic field can be determined from Ampére's law Eq.(1.2) (also see Section 3.3.1),

$$r^{-1}\frac{d(rB_\phi)}{dr} = \mu_0 j$$

and is given by

$$B_\phi(r) = \frac{\mu_0 I r}{2\pi a^2} \qquad 0 \le r \le a$$

$$= \frac{\mu_0 I}{2\pi r} \qquad r \le a$$

The positive terms in Eq.(2.23) are expansional forces while the negative terms represent beam compressional forces. In addition, it is assumed that the axially directed kinetic energy is

$$W_{\|kin} = \frac{1}{2}\gamma m N \beta^2 c^2 \tag{2.34}$$

Since Eq.(2.23) contains no axially directed energy, it must be argued that there are conversions or dissipation processes transferring a kinetic beam of energy of magnitude $W_{\|kin}$ into one or several kinds of energy expressed by the positive W elements in Eq.(2.23):

$$W_{\|kin} = W_{\perp kin} + W_{Ez} + W_{Bz} + W_k \tag{2.35}$$

2.5.1 The Bennett Relation

Balancing the thermokinetic and azimuthal compressional (pinch) energies in Eq.(2.23),

$$W_k - \frac{\mu_0}{8\pi} I^2 = 0, \tag{2.36}$$

yields the Bennett relation Eq.(1.9),

$$\frac{\mu_0 I^2}{4\pi} = 2NkT \tag{2.37}$$

If there is a uniform temperature $T = T_e = T_i$ and if the current density is uniform across the current channel cross-section, Eqs.(2.32), (2.33), and (2.37) yield a parabolic density distribution

$$n(r) = \frac{\mu_0 I^2}{4\pi^2 a^2 kT}\left(1 - \frac{r^2}{a^2}\right)$$

2.5.2 Alfvén Limiting Current

Equating the parallel beam kinetic energy to the pinch energy

$$W_{\|kin} - \frac{\mu_0}{8\pi} I^2 = 0 \tag{2.38}$$

yields the Alfvén limiting current

$$\boxed{I_A = 4\pi\varepsilon_0 m_e c^3 \beta\gamma/e = 17\,\beta\gamma \quad \text{kiloamperes}} \tag{2.39}$$

for an electron beam. This quantity was derived [Alfvén 1939] in order to determine at what current level in a cosmic ray beam the self-induced pinch field would turn the forward propagating electrons around. It should be noted that this limit is independent of any physical dimensions.

Lawson's (1959) interpretation of Eq.(2.39) is that the electron trajectories are beam-like when $I < I_A$ and they are plasma-like when $I > I_A$. In laboratory relativistic electron beam (REB) research, *Budker's parameter*

$$\nu_{Bud} = \pi a^2 \; n_b \; e^2 / mc^2 = N \; e^2 / mc^2 \tag{2.40}$$

where n_b is the electron density of the beam, finds wide application in beam and plasma accelerators. Yonas (1974) has interpreted the particle trajectories as beam-like for $\nu_{Bud} < \gamma$ and plasma-like for $\nu_{Bud} > \gamma$. The relationship between I_A and ν_{Bud} is

$$\nu_{Bud} / \gamma = I / I_A \tag{2.41}$$

The Alfvén limiting current Eq.(2.39) is a fundamental limit for a uniform beam, charge-neutralized ($f_e = 1$), with no magnetic neutralization ($f_m = 0$, Section 2.5.4), no rotational motion ($v_\phi = 0$), and no externally applied magnetic field ($B_z = 0$). By modifying these restrictions, it is possible, under certain circumstances, to propagate currents in excess of I_A.

2.5.3 Charge Neutralized Beam Propagation

Balancing the parallel kinetic, pinch, and radial electric field energies in Eq.(2.23) gives

$$W_{\|kin} - \frac{\mu_0}{8\pi} I^2 + \frac{1}{2} \pi a^2 \, \varepsilon_0 \, E_r^2(a) = 0 \tag{2.42}$$

which yields[2]

$$I_{max} = I_A \, \beta^2 / \left[\beta^2 - (1 - f_e)^2\right], \quad 0 \le f_e \le 1 \tag{2.43}$$

Depending on the amount of neutralization, the denominator in Eq.(2.43) can become small, and I_{max} can exceed I_A.

However, the unneutralized electron beam cannot even be injected into a drift space unless the space charge limiting current condition is satisfied. For a shearless electron beam this is [Bogdankevich and Rukhadze 1971]

$$I_{sc} = \frac{17\left(\gamma^{2/3} - 1\right)^{3/2}}{1 + 2 \ln (b/a)} \quad \text{kiloamperes} \tag{2.44}$$

where b is the radius of a conducting cylinder surrounding the drift space. Thus, in free space $I_{sc} \to 0$ and an unneutralized electron beam will not propagate but, instead, builds up a space charge cloud of electrons (a virtual cathode) which repels any further flow of electrons as a beam.

Moreover, the space charge limiting current is derived under the assumption of an infinitely large guide field B_z; no amount of magnetic field will improve beam propagation.

2.5.4 Current Neutralized Beam Propagation

For beam propagation in plasma, the electrostatic self-field E_r built up by the beam, efficiently drives a return current through the plasma, thus moderating the compressional term $\mu_0 I^2 / 8\pi$ in Eq.(2.23), so that

$$W_{\|kin} - \frac{\mu_0}{8\pi} I^2 \ (1 - f_m) + \frac{1}{2} \pi a^2 \ \varepsilon_0 \ E_r^2(a) = 0 \tag{2.45}$$

where the magnetic neutralization factor is

$$f_m \equiv |I_{return} / I| \tag{2.46}$$

From Eq.(2.45) the maximum current is

$$I_{max} = I_A \ \beta^2 / \left[\beta^2 \ (1 - f_m) - (1 - f_e)^2\right], \quad 0 \le f_e \le 1, \quad 0 \le f_m \le 1. \tag{2.47}$$

Thus, depending on the values of f_e and f_m, the denominator in Eq.(2.47) can approach zero and the maximum beam current can greatly exceed I_A. The effect of current neutralization is examined further in Section 2.9.1.

2.5.5 Discussion

When a charged particle beam propagates through plasma, the plasma ions can neutralize the beam space charge. When this occurs, $E_r \to 0$ and, as a result, the beam constricts because of its self-consistent pinch field B_ϕ. For beam currents in excess of the Alfvén limiting current, B_ϕ is sufficient to reverse the direction of the beam electron trajectories at the outer layer of the beam. However, depending on the plasma conductivity σ, the induction electric field at the head of the beam [due to $dB/dt \sim dI/dt$ in Eq.(1.1)] will produce a plasma current $I_p = -I_b$. Hence, the pinch field

$$B_\phi(r) = \frac{\mu_0}{2\pi r} [I_b \ (r) + I_p] \tag{2.48}$$

can vanish allowing the propagation of beam currents I_b in excess of I_A.

Because of the finite plasma conductivity, the current neutralization will eventually decay in a magnetic diffusion time τ_d given by Eq.(2.21). During this time a steady state condition exists in which no net self-fields act on the beam particles. While in a steady state, beam propagation is limited only by the classic macro-instabilities such as the sausage instability and the hose (kink) instability.

When the beam undergoes a small displacement, the magnetic field lags behind for times of the order τ_d. This causes a restoring force to push the beam back to its original position, leading to the well-known $m = 1$ (for a $e^{im\phi}$ azimuthal dependency) kink instability.

2.5.6 Beam Propagation Along an External Magnetic Field

An axially directed guide field B_z produces an azimuthal current component I_ϕ through Eq.(1.2). This modification to the conducting current follows by balancing the energies

$$W_{\|kin} - \frac{1}{2\mu_0} B_z^2 \pi a^2 - \frac{\mu_0}{8\pi} I^2 + \frac{1}{2} \varepsilon_0 E_r^2 \pi a^2 = 0 \tag{2.49}$$

In the absence of any background confining gas pressure $p(a)$, the maximum current is

$$I_{max} = I_\phi \beta^2 / \left[\beta^2 - (1 - f_e)^2\right] \tag{2.50}$$

For the case of an axial guide field, the axial current I_z is not limited to I_A and depends only on the strength of the balancing I_ϕ (B_z) current (magnetic field). In terms of the magnetic fields, the current flows as a beam when

$$B_z >> \frac{\left[(1 - f_e)^2 - \beta^2\right]^{1/2}}{\beta} B_\phi \tag{2.51}$$

Note that Eq.(2.44) still holds; that is, a cylindrical conductor around the electron beam is necessary for the beam to propagate.

Equation (2.51) finds application in accelerators such as the high-current betatron [Hammer and Rostocker 1970]. In spite of the high degree of axial stabilization of a charged particle beam because of B_z, appreciable *azimuthal* destabilization and filamentation can occur because of the diocotron effect (Section 1.7.3). This can be alleviated by bringing the metallic wall close to the beam.

2.5.7 Schönherr Whirl Stabilization

The transverse kinetic energy term $W_{\perp kin}$ in Eq.(2.23) explains an observation made long ago [Schönherr 1909]. High-current discharges conduct more current if the discharge is subject to an externally impressed rotation v_ϕ. This phenomena can also be expected in astronomical situations if the charged particle beam encounters a nonaxial component of a magnetic field line that imparts a spin motion to the beam or if a gas enters transversely to an arc discharge-like plasma.

2.5.8 The Carlqvist Relation

An expression having broad applicability to cosmic plasmas, due to Carlqvist (1988), may be obtained from Eq.(2.23) if the beam is taken to be cylindrical and in a rotationless and steady-state condition:

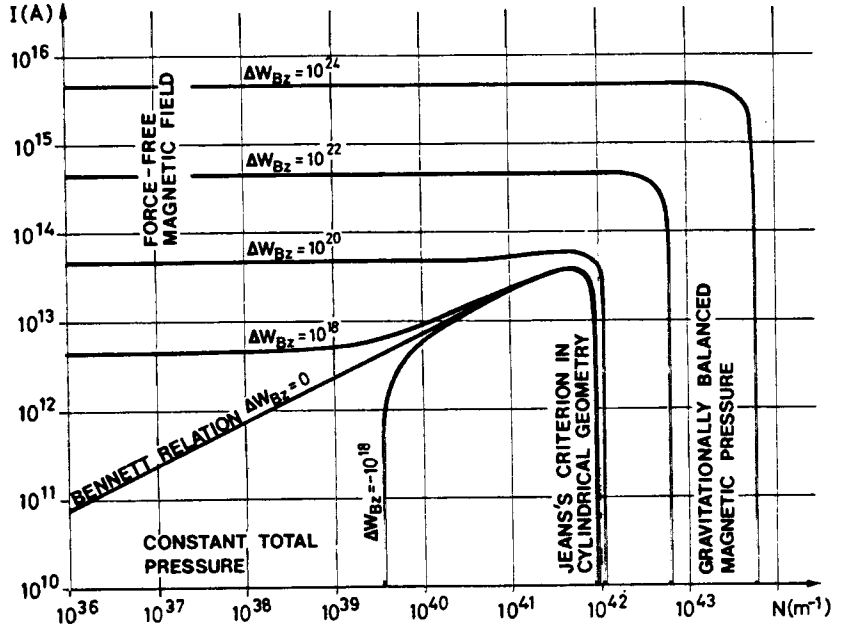

Figure 2.6. The total current I in a generalized Bennett pinch of cylindrical geometry as a function of the number of particles per unit length N. The temperature of the plasma is $T = 20$ K while the mean particle mass is m= 3×10^{-27} kg. It is assumed that the plasma does not rotate ($\omega = 0$) and that the kinetic pressure is much smaller at the border of the pinch than in the inner parts. the parameter of the curves is ΔW_{Bz}, representing the excess magnetic energy per unit length of the pinch due to an axial magnetic field B_z (courtesy of P. Carlqvist).

$$\frac{\mu_0}{8\pi} I^2(a) + \frac{1}{2} G \bar{m}^2 N^2(a) = \Delta W_{Bz} + \Delta W_k \tag{2.52}$$

Thus, in a straightforward and elegant way, the gravitational force has been included in the familiar Bennett relation. Through Eq.(2.52), the *Carlqvist Relation*, the relative importance of the electromagnetic force and the gravitational force may be determined for any given cosmic plasma situation. This relation will now be applied to the two commonest pinch geometries—the cylindrical pinch and the sheet pinch.

2.5.9 The Cylindrical Pinch

Consider the case of a dark interstellar cloud of hydrogen molecules ($\bar{m} = 3 \times 10^{-27}$ kg and $T = T_i = T_e = T_n = 20$ K). Carlqvist (1988) has given a graphical representation of the solution to Eq.(2.52) for these values and this is shown in Figure 2.6 for discrete values of ΔW_{Bz}. Several physically different regions are identified in this figure.

The region in the upper left-hand part of the figure is where the pinching force due to I and the magnetic pressure force due to B_z constitute the dominating forces. Equation (2.52) in this region reduces to

$$\frac{\mu_0}{8\pi} I^2 \approx \Delta W_{B_z} \tag{2.53}$$

representing a state of almost force-free magnetic field (Section 1.7.2).

Another important region is demarked by negative values of ΔW_{B_z}. In this region an outwardly directed kinetic pressure force is mainly balanced by an inwardly directed magnetic pressure force. Hence the total pressure is constant and Eq.(2.52) is approximately given by

$$NkT + \Delta W_{B_z} \approx 0 \tag{2.54}$$

For yet larger negative values of ΔW_{B_z}, the magnetic pressure force is neutralized by the gravitational force so that Eq.(2.52) reduces to

$$\frac{1}{2} G \overline{m}^2 N^2 \approx \Delta W_{B_z} \tag{2.55}$$

Another delineable region is where $\Delta W_{B_z} = 0$, where Eq.(2.52) reduces to the Bennett relation,

$$\frac{\mu_0}{8\pi} I^2 \approx \Delta W_k (n, T) \tag{2.56}$$

Another region of some interest is where the classic Bennett relation line turns over into an almost vertical segment. Here, the pinching force of the current may be neglected, leaving the kinetic pressure force to balance only the gravitational force so that

$$\frac{1}{2} G \overline{m}^2 N^2 \approx NkT \tag{2.57}$$

This is the Jeans's criterion in a cylindrical geometry.

The size or radius of the cylindrical pinch depends on the balancing forces. For the Bennett pinch Eq.(2.56) the equilibrium radius is

$$a \approx \frac{I}{2\pi} \sqrt{\frac{\mu_0}{2nkT}} \tag{2.58}$$

Küppers (1973) has investigated the case of a REB propagating through plasma. Space charge neutralization ($E_r = 0$) is maintained when $n_e + n_b = n_i$. For this case, the replacements $n \rightarrow n_b$ and $T \rightarrow T_b - T_e$ are made to $\Delta W_k (n, T)$, where T_b is the the beam temperature and T_e is the background plasma electron temperature. For the space charge neutralized REB,

$$a \approx \frac{I_b}{2\pi}\sqrt{\frac{\mu_0}{2n_b k(T_b - T_e)}} \tag{2.59}$$

Note that physically acceptable solutions for the equilibrium radius are obtained only when the beam temperature (in the axial direction for a cold beam) exceeds the plasma electron temperature.

From Eq.(2.53), the equilibrium radius of a pinch balanced by an internal field B_z is

$$a \approx \frac{\mu_0 I}{2\pi B_z} \tag{2.60}$$

2.5.10 The Sheet Pinch

The sheet pinch, which is the plane parallel analog of the cylindrical pinch, is a geometry of considerable importance in astrophysical plasmas. A current of density $j_z(x)$ flows in the z-direction in a symmetrical slab limited by the planes $x = \pm d$ (orthogonal coordinates x, y, z are adopted). This current induces a magnetic field $B_y(x)$. There also exists a magnetic field in the z–direction, $B_z(x)$, consistent with the current density $j_y(x)$. All quantities are supposed to vary with the x–coordinate only.

In a similar way as Eq.(2.52) was derived, Carlqvist (1988) uses the force equation (without the centrifugal term) to obtain the relation

$$\mu_0 I^2(d) + 4\pi G\overline{m}^2 N^2(d) = 8\left(\Delta p_k + \Delta p_{B_z}\right) \tag{2.61}$$

for the one-dimensional, charge neutral pinch where

$$I\ (d) = 2\int_0^d j_z\, dx \tag{2.62}$$

is the current per unit length of the slab, and

$$N(d) = 2\int_0^d (n_e + n_i + n_n)\, dx \tag{2.63}$$

is the number of particles per unit area of the slab. The kinetic pressure and magnetic pressure difference terms in the slab are, respectively, given by

$$\Delta p_k = p_k(0) - p_k(d) \tag{2.64}$$

$$\Delta p_{B_z} = p_{B_z}(0) - p_{B_z}(d) \tag{2.65}$$

Equation (2.61) is the one-dimensional analog of (2.52) and Figure 2.7 is its graphical solution using the same parameter values as in Figure 2.6. Comparison of Figures 2.6 and 2.7 reveals a striking similarity between the behavior of cylindrical and sheet pinches.

By means of the theory discussed in Section 2.5, in the next section we shall study the physical conditions in a few different, current-carrying, cosmic plasmas.

2.6 Application of the Carlqvist Relation

2.6.1 Birkeland Currents in Earth's Magnetosphere

Magnetometer measurements from rockets and satellites show that Birkeland currents often exist in sheets in the auroral zones, where the current density may be as large as $j_{\parallel} \approx 10^{-4}$ A m^{-2}. The thickness of such sheets is found to range from a few kilometers to several hundred kilometers. Often the sheets exist in pairs with oppositely directed currents.

Consider a model of a Birkeland current with a current density $j_z \approx 3 \times 10^{-5}$ A m^{-2} flowing in a magnetospheric plasma slab of half-thickness $d = 10^4$ m [Carlqvist 1988]. The mean mass of

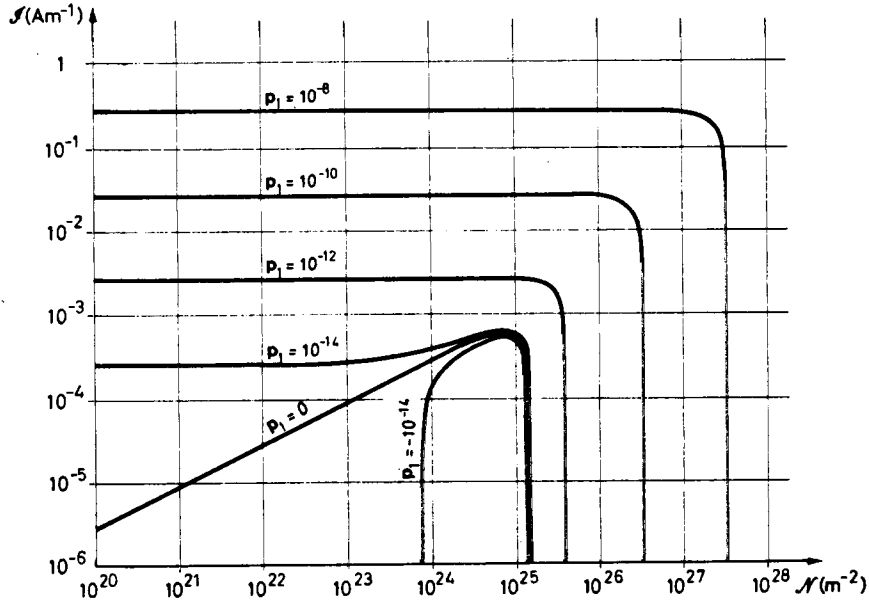

Figure 2.7. The current per unit length I as a function of the number of particles N in a generalized Bennett pinch of plane parallel geometry forming a slab. The temperature and mean particle mass are the same as in Figure 2.6. It is assumed that $n(0) \approx N/d$. The parameter of the curves is $p_1 = \Delta p_{B_z} - p_k(d)$ where $p_k(d)$ is the kinetic pressure at the border of the slab while Δp_{B_z} denotes the difference of the magnetic pressure due to B_z between the center of the slab and the borders (courtesy of P. Carlqvist).

the electrons and protons in the slab is taken to be $\overline{m} \approx 10^{-27}$ kg. At an altitude of a few thousand kilometers above the earth, $n_e = n_i \approx 10^{10}\,\mathrm{m}^{-3}$, $T \approx 2 \times 10^3$ K, and $B_z \approx 4 \times 10^{-5}$ T. Substituting these values into Eqs.(2.62) and (2.63), gives

$$I(d) \approx 6 \times 10^{-1}\ \mathrm{A\,m^{-1}}$$
$$N(d) \approx 4 \times 10^{14}\ \mathrm{m^{-2}}$$

Under steady state conditions, Eq.(2.61) is applicable and its terms have the magnitudes:

$$\mu_0 I^2(d) \approx 5 \times 10^{-7}\ \mathrm{Pa}$$
$$4\pi G \overline{m}^2 N^2(d) \approx 1 \times 10^{-34}\ \mathrm{Pa}$$
$$8\Delta p_k < 8p_k(0) \approx 4 \times 10^{-9}\ \mathrm{Pa}$$
$$8\Delta p_{Bz} < 8p_{Bz}(0) \approx 5 \times 10^{-3}\ \mathrm{Pa}$$

Hence, the gravitational and kinetic pressure terms may be neglected with respect to the pinching current and B_z pressure. These values for $N(d)$ and Δp_{Bz} pertain to the lower far-left region in Figure 2.7, corresponding to the force-free magnetic field configuration (Section 1.7.2).

For a strong circular aurora, 5,000 km in diameter (Figure 1.18a), the total current is $I = I(d)\,2\pi r \approx 7$ MA.

2.6.2 Currents in the Solar Atmosphere

The solar atmosphere consists of a highly conducting plasma in which vertical currents of about 10^{11}–10^{12} A are common in active regions where solar flares occur. For a current of $I = 3 \times 10^{11}$ A flowing in a filament of radius $a \leq 10^6$ m, $j_z \approx 0.1\ \mathrm{A\,m^{-2}}$. The length of the filament is $l \approx 10^8$ m and passes mainly through the lower corona in a loop connecting two foot-prints in the photosphere. The coronal plasma density and temperature is taken to be $n_e = n_i \leq 10^{16}\,\mathrm{m^{-3}}$ and $T \approx 100$ eV (10^6 K) (Table 1.3) and uniformly distributed across the filament so that differential kinetic pressure term $\Delta W_k(a)$ is negligible. Hence,

$$I(a) \approx 3 \times 10^{11}\ \mathrm{A}$$
$$N(a) \approx 6 \times 10^{28}\ \mathrm{m^{-1}}$$

Applying Eq.(2.52), the magnitudes of the remaining terms are

$$\mu_0 I^2 / 8\pi \approx 4 \times 10^{15}\ \mathrm{J\,m^{-1}}$$
$$G\overline{m}^2 N^2 / 2 \approx 3 \times 10^{-8}\ \mathrm{J\,m^{-1}}$$
$$\Delta W_{Bz}(a) < W_{Bz} \approx 1 \times 10^{17}\ \mathrm{J\,m^{-1}}$$

for a magnetic field $B_z \approx 0.1$ T within the filament. Gravity is negligible and a force-free magnetic field configuration exists.

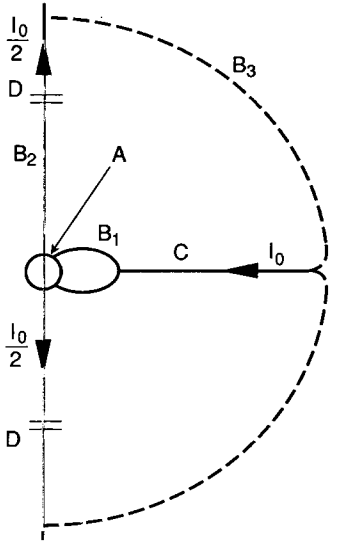

Figure 2.8. Heliospheric circuit. The sun acts as a unipolar inductor producing a current which goes outward along both the axes and inward in the equatorial plane C and along the magnetic field lines B_1. The current closes at large distances B_3.

2.6.3 Heliospheric Currents

The heliospheric current system [Alfvén 1981] consists of the sun as a unipolar generator with axial currents flowing out of (or into, depending on the polarity of the sun) the solar polar regions. These currents fan out and close at great distances from the sun, probably near the heliopause. The return current flows back towards (or away from) the sun in a thin and wavy layer near the equatorial plane, eventually dividing and terminating at high latitudes on the northern and southern hemispheres, where the currents are then conducted across the sun (Figure 2.8). The magnitude of the total current in each of the polar regions is $I_p \approx 1.5 \times 10^9$ A.

Whether or not the polar current is diffuse or filamentary is an important problem for cosmic plasmas.

Example 2.1 Polar currents balanced by axial magnetic fields. Consider the case of M filamentary currents each containing an axial magnetic field $B_z \approx 30 \times 10^{-4}$ T (Table 1.3). Each current conducts I/M amperes so that, if $M = 1000$, a filamental current is $I = 1.5 \times 10^6$ A. According to Eq.(2.60), the radius of each filament is $a \approx 100$ m. If the filaments are approximately equally spaced a diameter's distance from one another, they form a tube of radius of the order of 5 km, each with a current density $j_z \approx 20$ A/m^2. If, on the other hand $M = 1$, $I = 1.5 \times 10^9$ A and $a \approx 100$ km. For this diffuse current case, $j_z \approx 0.05$ A/m^2.

Example 2.2 Polar currents in an axial magnetic field balanced by the thermokinetic plasma. Consider the conducting path to be plasma with $n = 2 \times 10^{15}$ m^{-3} and $T = 100$ eV (10^6 K) (Table 1.3). For this case, $M = 1000$ filaments each of which conducts 1.5×10^6 A and, according to Eq.(2.58), each has a Bennett radius $a \approx 1.5$ km. The filaments fill a tube of radius of the order of 50 km and each has a current density $j_z \approx 0.2$ A/m^2. If $M = 1$, $I = 1.5 \times 10^9$ A and $a \approx 1500$ km. For this diffuse current case, $j_z \approx 2 \times 10^{-4}$ A/m^2.

2.6.4 Currents in the Interstellar Medium

Currents in the interstellar medium may be one or two orders of magnitude stronger than solar currents. Consider first a single interstellar cloud of density $n \approx 10^7$ m^{-3}, linear extent $l_c \sim 10^{16}$ m, and temperature $T \approx 10$ K. The total mass $M_c \approx 2 \times 10^{32}$ kg corresponds to a single solar mass. Hence, representative values for current and number density per unit length are

$$I = 10^{13} \text{ A}$$
$$N = 10^{39} \text{ m}^{-1}$$

Under steady state conditions, the magnitude of the terms in Eq.(2.52) are

$$\mu_0 I^2 / 8\pi \approx 5 \times 10^{18} \text{ J m}^{-1}$$
$$G\bar{m}^2 N^2 / 2 \approx 3.3 \times 10^{13} \text{ J m}^{-1}$$
$$\Delta W_k < W_k \approx 1.4 \times 10^{17} \text{ J m}^{-1}$$

so that the Bennett relation Eq.(2.56) is applicable.

Consider now an interstellar cloud of density $n \approx 10^8$ m^{-3}, linear extent $l_c \sim 10^{17}$ m, and temperature $T \approx 10$ K. These values are typical of the Orion nebula, where the total mass $M_c \approx 2 \times 10^{32}$ kg corresponds to a hundred solar masses. Hence,

$$I = 10^{14} \text{ A}$$
$$N = 10^{42} \text{ m}^{-1}$$

Under steady state conditions, the magnitude of the terms in Eq.(2.52) are as follows:

$$\mu_0 I^2 / 8\pi \approx 5 \times 10^{20} \text{ J m}^{-1}$$
$$G\bar{m}^2 N^2 / 2 \approx 3.3 \times 10^{19} \text{ J m}^{-1}$$
$$\Delta W_k < W_k \approx 1.4 \times 10^{20} \text{ J m}^{-1}$$

That is, the pinch, gravitational, and kinetic forces are approximately balanced. The two cases illustrated above are representative of particular values found in Figure 2.6.

2.6.5 Currents in the Galactic Medium

By extrapolating the size and strength of magnetospheric currents to galaxies, Alfvén (1977) suggests a number of confined current regions that flow through interstellar clouds and assist in their formation. For example, a galactic magnetic field of the order $B_G \sim 10^{-9}$–10^{-10} T associated with a galactic dimension of 10^{20}–10^{21} m suggests the galactic current be of the order $I_G = 10^{17}$–10^{19} A.

As a natural extension of the size hierarchy in cosmic plasmas, these currents are thought to have an axial component parallel to an axial galactic magnetic field, in addition to the ring or azimuthal current component, so that the galactic currents are galactic-dimensioned Birkeland currents [Peratt and Green 1983]. From Section 1.2.6 (also see Example 6.3), $n_e = 2 \times 10^3$ m^{-3}, $T_\perp = 3$ keV (3×10^7 K), and $B_z = 2 \times 10^{-8}$ T. The radius is $a \approx 17$ kpc (0.5×10^{21} m). Hence,

$$I = 2.5 \times 10^{19} \text{ A}$$
$$N = 2.9 \times 10^{45} \text{ m}^{-1}$$

Under steady state conditions, the magnitude of the terms in Eq.(2.52) are

$$\mu_0 I^2 / 8\pi \approx 3 \times 10^{31} \text{ J m}^{-1}$$
$$G\bar{m}^2 N^2 / 2 \approx 2.6 \times 10^{26} \text{ J m}^{-1}$$
$$\Delta W_k < W_k \approx 1.3 \times 10^{30} \text{ J m}^{-1}$$

where it has been assumed that the galactic currents are imbedded in B_z so that ΔW_{Bz} is negligible. Hence, the galactic pinch is balanced by the thermokinetic pressure of the plasma it contains and, to a lesser extent, by gravity.

For a galactic field $B \sim 10^{-8}$ T over a volume $V \sim 10^{63}$ m^3 ($l_G \sim a_G \sim 10^{21}$ m), the magnetostatic energy Eq.(3.41) is $W_B \sim 10^{53}$ J.

2.6.6 Currents in the Intergalactic Medium

One of the most compelling pieces of evidence for the existence of supercluster-sized Birkeland currents comes from the discovery of faint supercluster-scale radio emission at 326 MHz between the Coma cluster of galaxies and the Abell 1367 cluster [Kim et al. 1989]. The radiation's synchrotron origin implies the existence of a large-scale intercluster magnetic field with an estimated strength of 0.3–0.6 $\times 10^{-10}$ T (0.3–0.6 μG). For the linear dimension l of the source, ~1.5 Mpc, the current $I = \mu_0^{-1} A \left| \nabla \times \mathbf{B} \right|$ to produce a field of this magnitude is $I \sim l B / \mu_0 \sim 0.5 \times 10^{19}$ A.

Further evidence for such currents is examined in Chapters 3, 6, and 7.

2.7 Basic Fluid and Beam Instabilities

2.7.1 Jeans Condition for Gravitational Instability

Consider matter in the gaseous, rather than plasma, state. Further assume that the gas is nonmagnetized, static, and uniform. Take the zero-order velocity v_0 to be zero, and the mass density ρ_0 and pressure p_0 to be constant. Next assume a density perturbation of strength ρ_1 / ρ_0 such that the mass density is $\rho_m = \rho_0 + \rho_1$ and the velocity $v = v_1$. Under these assumptions, Eqs.(2.15) and (2.13) may be linearized to obtain

$$\frac{\partial \rho_1}{\partial t} + \rho_0 \nabla \cdot \mathbf{v}_1 = 0 \tag{2.66}$$

$$\rho_0 \frac{\partial \mathbf{v}_1}{\partial t} = -\nabla p_1 - \rho_0 \nabla \varphi_{G1} \tag{2.67}$$

For an isothermal process in an ideal gas $p_1 = kT\rho_1 / M$, where M is the total mass of the molecular gas. From Poisson's equation

$$\nabla^2 \phi_{G1} = 4\pi G \rho_1 \tag{2.68}$$

Equations (2.66) - (2.68) may be combined to form a wave equation

$$\frac{\partial^2 \rho_1}{\partial t^2} = \frac{kT}{M} \nabla^2 \rho_1 + 4\pi G \rho_0 \rho_1 \tag{2.69}$$

Equation (2.69) has the plane wave solution

$$\rho_1 = \rho_0 e^{i(k r - \omega t)} \tag{2.70}$$

where $k = 2\pi / \lambda$ is the wavenumber and the frequency ω is given by

$$\omega^2 = k^2 v_s^2 - 4\pi G \rho_0 \tag{2.71}$$

where

$$v_s = \sqrt{kT / M} \tag{2.72}$$

is identified as the velocity of sound in the gas.

One of the roots of Eq.(2.71) is positive imaginary

$$\omega = +i\sqrt{4\pi G\rho_0 - k^2 v_s^2} \tag{2.73}$$

so that Eq.(2.70) is an exponentially growing perturbation with growth rate

$$\Gamma = \sqrt{4\pi G\rho_0 - k^2 v_s^2} \tag{2.74}$$

when

$$k^2 v_s^2 = \left(\frac{2\pi}{\lambda}\right)^2 v_s^2 < 4\pi G\rho_0 \tag{2.75}$$

That is, the gas is unstable to density fluctuations with a wavelength λ greater than the critical wavelength [Jeans 1902]

$$\lambda_J = \sqrt{\frac{\pi kT}{GM\rho_0}} \tag{2.76}$$

The velocity of propagation V_J of the density perturbation is given by [Jeans 1902]

$$V_J = k\omega = v_s \sqrt{1 - \frac{G\rho_0 \lambda^2}{\pi v_s^2}} \tag{2.77}$$

Based on the assumption leading to Eqs.(2.66) and (2.67), Jeans found that a spherical gas distribution whose diameter was larger than λ_J, would contract continuously due to G. The critical mass of such a sphere of gas is $M_J = \frac{\pi}{6}\rho_0 \lambda_J^3$. It should be noted that these results are only applicable for a medium in which the Lundquist parameter Eq.(1.6) is of order unity or less.

2.7.2 Two-Stream (Buneman) Instability

Consider a plasma in which the ions are stationary $v_{i0} = 0$ and the electrons have a velocity $\mathbf{V}_0$ relative to the ions. Let the plasma be cold, $T = T_e = T_i = 0$ and assume $\mathbf{B}_0 = 0$. Under these assumptions, Eqs.(2.15) and (2.13) may be linearized to yield

$$\frac{\partial n_{i1}}{\partial t} + n_0 \nabla \cdot \mathbf{v}_{i1} = 0 \tag{2.78}$$

$$\frac{\partial n_{e1}}{\partial t} + n_0 \nabla \cdot \mathbf{v}_{e1} + (\mathbf{V}_0 \cdot \nabla) n_{e1} = 0 \tag{2.79}$$

$$n_0 m_i \frac{d\mathbf{v}_{i1}}{dt} = n_0 m_i \frac{\partial \mathbf{v}_{i1}}{\partial t} = e n_0 E_1 \tag{2.80}$$

$$n_0 m_e \frac{d\mathbf{v}_{e1}}{dt} = n_0 m_e \left[\frac{\partial \mathbf{v}_{e1}}{\partial t} + (\mathbf{V}_0 \cdot \nabla)\mathbf{v}_{e1}\right] = -e n_0 E_1 \tag{2.81}$$

where $n_{i0} = n_{e0} = n_0$. Note that in Eq.(2.78) use has been made of $\nabla n_0 = \mathbf{v}_{i0} = 0$ while in Eq.(2.80) $(\mathbf{v}_{i0} \cdot \nabla)\mathbf{v}_{i1} = 0$. For electrostatic waves $\mathbf{E}_1 = \hat{\mathbf{z}}\, E\, e^{i(kz - \omega t)}$, and Eqs.(2.78)–(2.81) may be written as

$$-i\omega n_{i1} + ik n_0 \mathbf{v}_{i1} = 0 \tag{2.82}$$

$$(-i\omega + ikV_0) n_{e1} + ik n_0 \mathbf{v}_{e1} = 0 \tag{2.83}$$

$$-i\omega\, n_0 m_i \mathbf{v}_{i1} = e n_0 E_1 \tag{2.84}$$

$$n_0 m_e (-i\omega + ikV_0)\mathbf{v}_{e1} = -e n_0 E_1 \tag{2.85}$$

Solving Eqs.(2.82)–(2.85) for the velocities and densities gives

$$\mathbf{v}_{i1} = \frac{ie}{m_i \omega} E_1 \tag{2.86}$$

$$\mathbf{v}_{e1} = \frac{-ie}{m_e} \frac{E_1}{(\omega - kV_0)} \tag{2.87}$$

$$n_{i1} = \frac{ie n_0 k}{m_i \omega^2} E_1 \tag{2.88}$$

$$n_{e1} = \frac{-ie n_0 k}{m_e} \frac{E_1}{(\omega - kV_0)^2} \tag{2.89}$$

Because the unstable waves are high-frequency plasma oscillations, the plasma approximation (Section 2.4.1) cannot be used, and the electrostatic field must be obtained from Poisson's equation (1.3):

$$\varepsilon_0 \nabla \cdot \mathbf{E}_1 = e(n_{i1} - n_{e1}) \tag{2.90}$$

Substituting $\nabla \cdot \mathbf{E}_1 = ikE_1$, Eq.(2.88), and Eq.(2.89) into Eq.(2.90), yields the dispersion relation,

$$1 = \frac{\omega_{pi}^2}{\omega^2} + \frac{\omega_{pe}^2}{(\omega - kV_0)^2} \tag{2.91}$$

Equation (2.91) has four roots and, under certain conditions, two of these are complex conjugate. The location of the complex root having a positive imaginary component is given by [Krall and Trivelpiece 1973]

$$\omega' = kV_0 \left[\frac{(\omega_{pe}/\omega_{pi})^{2/3}}{(\omega_{pe}/\omega_{pi})^{2/3} + 1} \right] \tag{2.92}$$

The condition for instability is that the right-hand side of Eq.(2.91) be greater than 1 at $\omega = \omega'$, and is

$$|kV_0|^2 < \omega_{pe} \left[1 + (\omega_{pi}/\omega_{pe})^{2/3} \right]^3 \tag{2.93}$$

This is the *two-stream*, or *Buneman*, instability [Buneman 1959]. Since the sign of the charge does not appear, Eq.(2.93) can be equally well applied to two electron streams in a fixed neutralizing ion background, replacing ω_{pi}/ω_{pe} by $\omega_{pe1}/\omega_{pe2}$.[3] The introduction of thermal effects becomes important only if the thermal velocities are of the order of V_0, in which case the flow can hardly be classified a beam.

The physical interpretation of Eq.(2.91) is that, because of the Doppler shift of the plasma oscillations, the ion and electron plasma frequencies can coincide in the laboratory frame only if kV_0 has the proper value. The ion and electron density fluctuations can then satisfy Poisson's equation. The electron oscillations have negative energy; they draw energy from the kinetic energy of the electrons.[4] Therefore, the negative energy electron waves and the positive energy ion waves both can grow while the total energy of the system remains constant. This type of instability finds application in high-power microwave generation in relativistic klystrons [Peratt and Kwan 1990]. A REB is velocity modulated by an rf signal, thereby producing bunches of accelerated electrons that pass through the slower velocity or deaccelerated electrons. This produces a two-stream condition. As the bunches pass through a microwave resonator, they excite the natural mode of the cavity to produce microwave power.

In space and cosmic plasmas, the two stream condition often exists to produce electromagnetic radiation (albeit at efficiencies far less than laboratory devices), and may also be the source of double layers in Birkeland currents (Chapter 5).

2.7.3 Sausage and Kink Instabilities

The simple pinch has a number of serious instabilities [Shrafranov 1957]. The sausage ($m = 0$) instability occurs periodically along the pinch where the magnetic pressure $B_\phi^2 / 2\mu_0$ becomes greater. This causes bulges to appear which result in even greater inward pressure between them. Ultimately, if the axial current is strong enough, the pinch can collapse into force-free magnetic plasmoids.

The kink ($m = 1$) instability produces a helical mode in the pinch. This most often occures when a strong axial magnetic guide field is present, that is, the pinched plasma is a Birkeland current. The simulated time evolution of the kink instability is discussed in Section 2.9.2.

2.8 Laboratory Simulation of Cosmic Plasma Processes

The rapid development of high-voltage pulsed power technology in the 1970s and 1980s has made it possible, for the first time, to investigate the intense currents, high voltages, and energetic particles found in space and cosmic plasma. Megaamperes of current in pulsed beams of electrons and ions with particle kinetic energies in the range from ~100 keV to several hundred MeV have been achieved. Although this technology was originally developed for materials testing, X radiography, and nuclear weapon effects simulation, it has found widespread use in such diverse fields as thermonuclear fusion, high-power microwave generation, collective ion acceleration, laser excitation, and laboratory astrophysics.

A multi-terawatt pulsed-power generator may typically consist of an array of capacitor banks (called a "Marx bank"), or many kilograms of high explosive on a magnetic-compression-generator, driving a coaxial pulseline (Figure 2.9).[5] A diode consisting of an outer anode and a cathode (terminating the inner coaxial conductor) is attached to the water pulseline through a coaxial vacuum transmission line. The purpose of the pulseline is to shorten the microseconds-long-pulse generated by the Marx bank, which may contain megajoules of energy, to a 30–60 nanosecond-long-pulse at the diode, thereby producing a power amplification (watts = joules per second). In this way, space and astrophysical magnitude quantities are generated: megaamperes of current, megavolts of potential differences, megaelectronvolt particle energies, and terawatts of power.

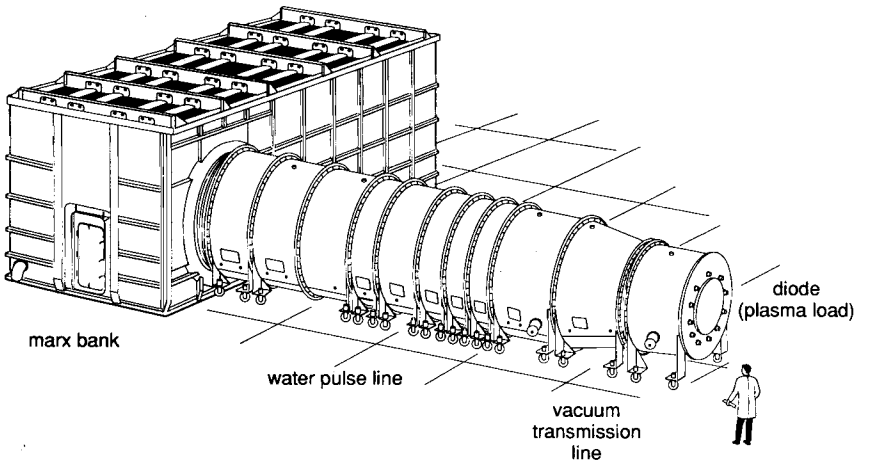

Figure 2.9. A multi-terawatt pulsed-power generator. The diode, that contains the plasma load, is located at the end of the cylindrical, coaxial, pulse shaping line.

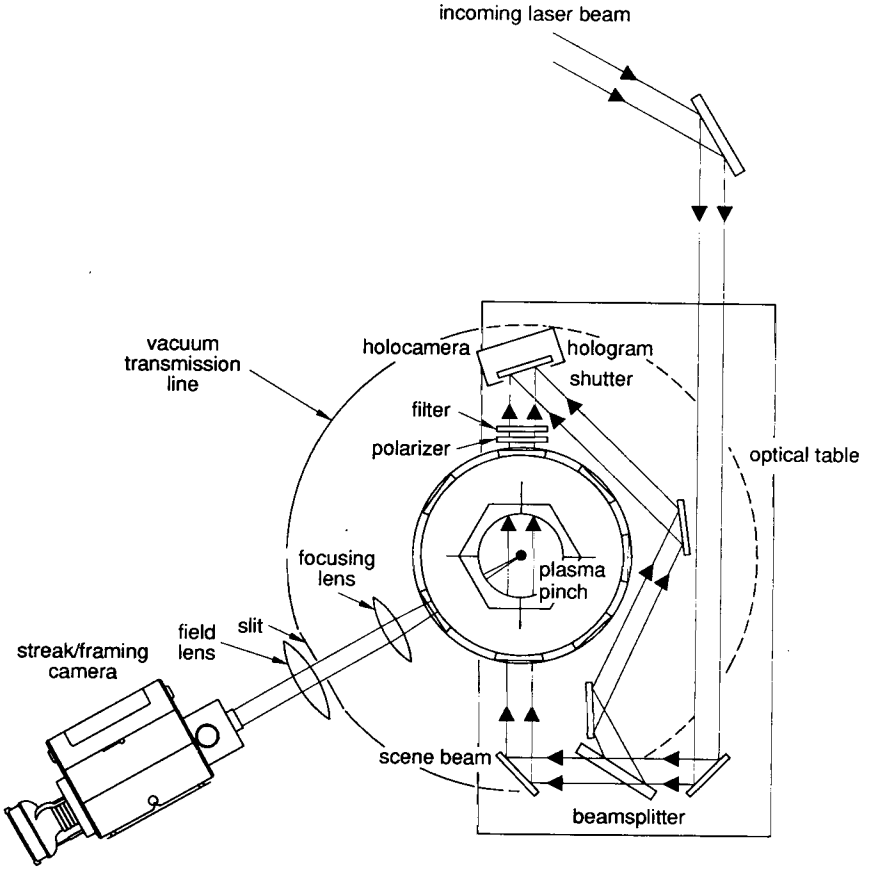

Figure 2.10. Diagnostics setup on pulsed-power generator diode. Shown are the pulsed-laser holography and framing camera setups.

2.8.1 High-Current Plasma Pinches

A plasma pinch can be created by attaching thin (few microns thick) wires or thin cylindrical foils between the cathode and anode, or else injecting gas between the cathode and anode at the time of pulse arrival.

Unlike most astrophysical pinches, the laboratory pinch is available to *in situ* measurement and study. The magnetohydrodynamic evolution is recorded using streak and framing cameras to record the bulk plasma motion, pulsed-laser holography and shadowgraphy to study time resolved morphology, and Faraday rotation measurements to plot magnetic field vectors (Figure

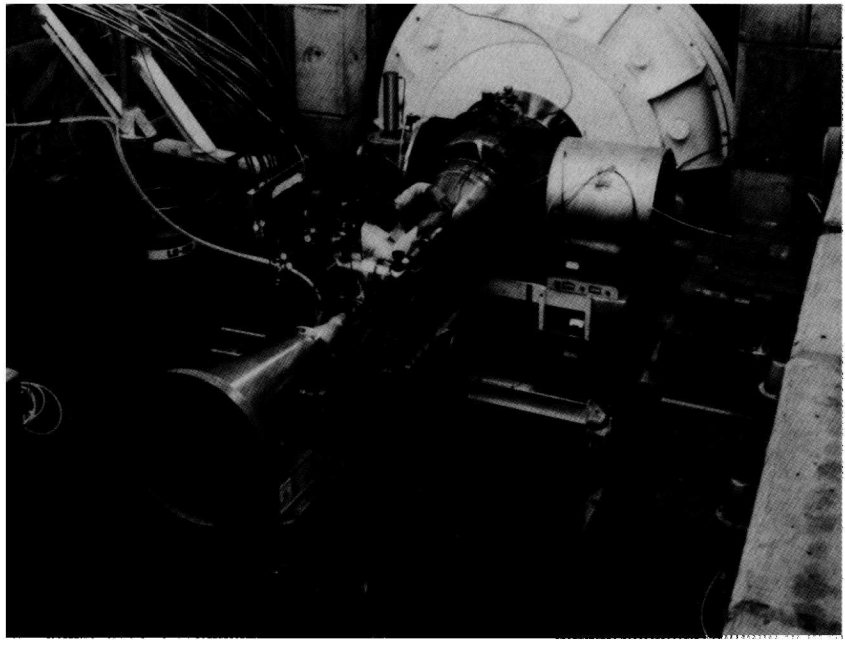

Figure 2.11. Diagnostics setup to study microwave emission. The microwave horn is attached to the generator diode.

2.10). The radiation history is recorded using X ray detectors, spectrum analyzers, pin-hole X ray cameras, and microwave antennas (Figure 2.11).

Figure 2.12 shows the time history of a jet of argon gas injected through the cathode. At time 7 ns the gas is ionized by the arrival of the MV pulse. The images, recorded in soft X rays, show the flaring out of the hollow gas towards the anode. At 14 ns the gas is fully ionized and the plasma conduction current is nearly 4 MA, causing the plasma to pinch. The inward compression of plasma is halted when the pinch undergoes a transformation to a force-free state, producing the "plasmoids" recorded at 21 ns.[6] These plasmoids then pair together, sometimes producing spiral configurations such as that (barely discernible) at 28 ns.

A detailed study of plasmoid interaction was carried out by Bostick (1956, 1957). Figure 2.13 shows the time history of spiral formation from plasmoids produced by plasma guns (Section 4.6.2) fired at each other across a magnetic field.

The unique possibility of plasma pinches to create ultradense matter, such as that in the interiors of stars, is investigated in some detail by Meirovich (1984).

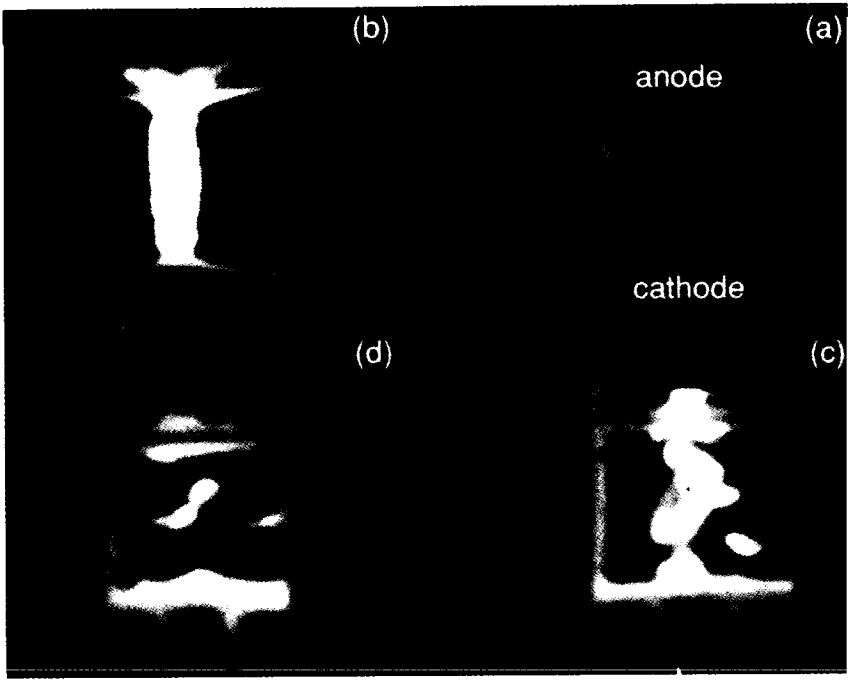

Figure 2.12. Evolution of a plasma pinch produced by fully ionized argon gas. These photos were recorded in soft X rays by a framing camera. The cathode is at the bottom of each frame while the anode is at the top.

2.8.2 Laboratory Aurora Simulations

The magnetized sheet electron beam has been studied in some detail in a very careful set of experiments carried out by Webster (1957). Webster was able to produce laboratory analogs of the polar aurora in a small, vacuum, anode-cathode arrangement in which currents as low as 58 μA were conducted and detected (Figure 1.20). The experimental setup consisted of a small vacuum tube (Figure 2.14) that launched a 0.1 cm × 1.2 cm flat sheet electron beam by means of a slotted grid disk in front of the cathode. The beam traveled 9.2 cm parallel to a 71 G axial magnetic field until it struck a fluorescent screen anode. The fluorescent screen was made of a thin coating (1 mg/cm^2) of ZnO phosphor.

Figure 2.15 depicts a series of single-frame photographs of the phosphor screen showing the beam shape at the anode as the beam voltage was increased. Here we see that the sheet beam rotates as a rigid rod through an angle of about 30°. Beyond this angle, the beam begins to fold into charge bunches, producing vortex patterns on the phosphorus plate. At a certain critical voltage, the vortices disrupt, producing a violent oscillation. These oscillations have a complex waveform indicating a rather broadband frequency distribution. The bandwidth increases rapidly with beam voltage.

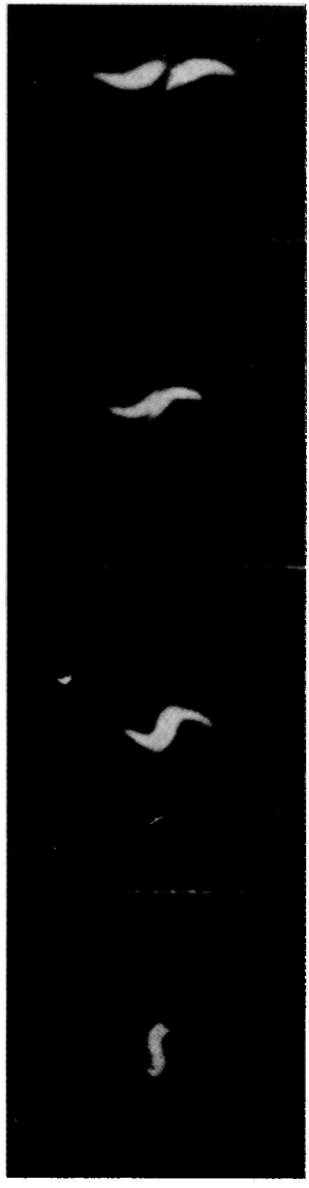

Figure 2.13. The evolution of two plasmoids fired at each other across a magnetic field (courtesy W. Bostick).

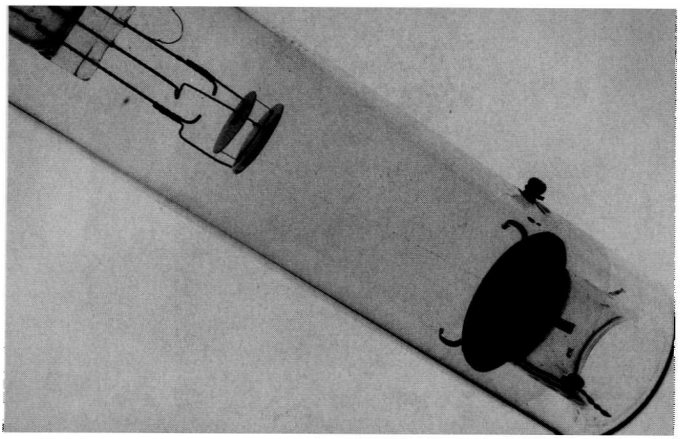

Figure 2.14. Vacuum electron tube used to simulate the aurora. The total length of the tube is about 20 cm (courtesy of H. Webster).

2.9 The Particle-in-Cell Simulation of Beams and Birkeland Currents

Even before its application to plasmas, the particle-in-cell technique was applied to the study of electron beams in vacuum (Chapter 8). This section is concerned with the particle-in-cell simulation of electron beams, in the presence or absence of an external magnetic field, propagating through plasma. The beam may be a solid or hollow cylinder, or a planar sheet, a geometry that happens to be of particular interest to the study of the aurora or of vacuum devices. Thin sheet beams produced by electrons ejected from cathodes along magnetic lines of force have found a multiple applications on earth (e.g., in cross-field microwave generators, backward-wave amplifiers, and in multi-gapped particle accelerators). Furthermore, solid cylindrical beams of electrons traveling a sufficient distance along a magnetic field line can become cylindrical-sheet beams due to a hollowing instability [Ekdahl 1987]. For these applications, the particle-in-cell simulation (PIC) technique has been often used to study the dynamics of sheets of charged particles [Hallinan 1976, Jones and Mostrom 1981]. This offers an opportunity to benchmark the simulation against physical data.

A simulation of complex phenomenon is generally given little credence until it is "benchmarked" against physical measurements. For this reason, laboratory measurements and the PIC approach often create a synergism in understanding the problem at hand. This approach works best when high quality diagnostics methods are available to guide the simulation.

The beams and Birkeland filaments simulated in Section 2.9 will be found to exhibit a number of properties which will be pursued throughout the remainder of this book: pinching of plasma in the presence of a field-aligned electric field (Chapters 4 and 5), uniform bulk rotation of the plasma particles indicative of force-free plasma interiors (when the external fields are turned off or become negligible), and the release of electromagnetic radiation via the synchrotron process (Chapter 6).

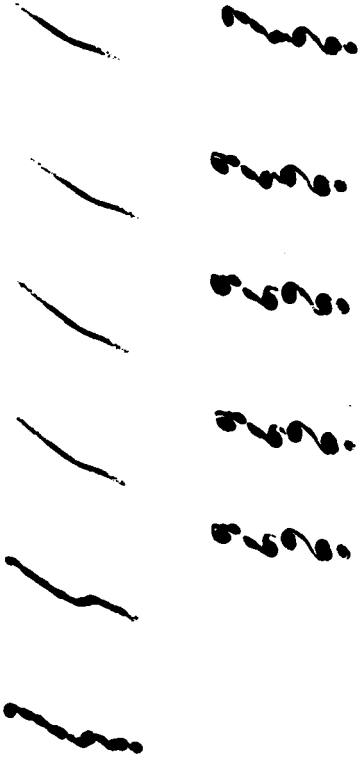

Figure 2.15. Laboratory simulated aurora. Voltage (current) increases continuously from top to bottom in each column.

2.9.1 Charge and Current Neutralized Beam Propagation in Plasma

Consider a cold plasma of electrons and ions of density $n_p = 0.28$ cm^{-3}. A beam of electrons of radius $a = 100$ km at density $n_b/n_p = 0.003$ and a risetime of 7 ms propagates from the left in a simulation region of dimension 500 km × 300 km This problem was simulated with the particle code ISIS (Figure 2.16). (For this problem the plasma skin depth parameter $\lambda_E = c / \omega_p$ is 10 km.) The beam is mildly-relativistic with $\beta\gamma = 0.2$. Because of the background plasma, the beam is charge neutralized so that $f_e = 1$ and the beam propagates without diverging.

As the beam propagates, a return current is set up within the beam by the plasma electrons. [The electron beam flow is to the right so the beam current is to the left, i.e., a negative value. The return current has a positive value.] Because of the return current, the beam is very nearly current neutralized, $f_m \approx 1$. The nonneutralized part of the axial current j_z and the nonzero azimuthal field B_ϕ are largely localized within a few plasma skin depths λ_E at the beam edge (Figures 2.16 c,d)

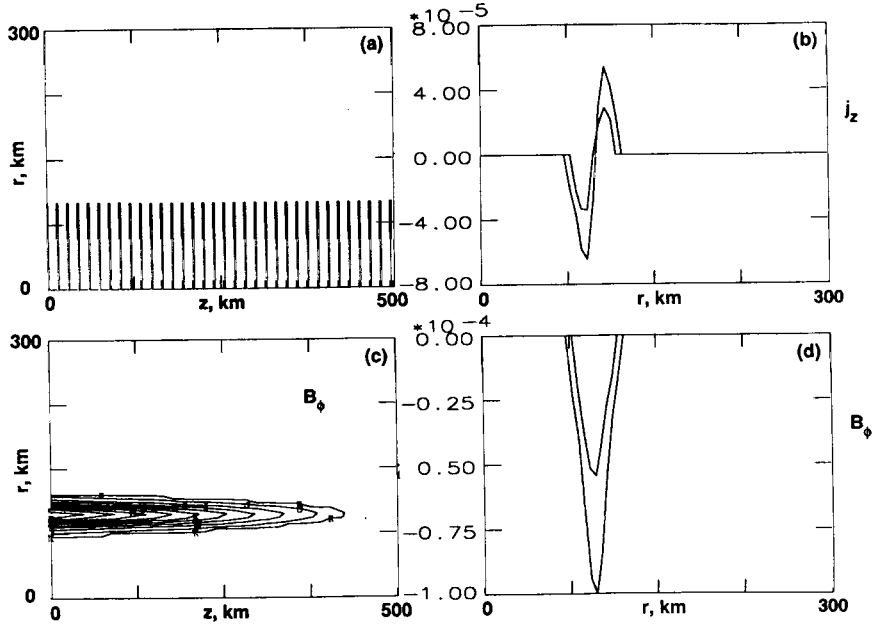

Figure 2.16. (a) Electron beam profile along the axial dimension. The beam propagates from left to right through a plasma background. (b) Current density versus radius. The ordinate is in units of $17\ kA\ /\ 4\pi\lambda_E^2 = 1.35 \times 10^{-5}$ A/m^2. The return current is equal to the beam current out to a radius of 75 km. (c) Self magnetic field profiles. (d) Self field versus radius. The ordinate is in units of $\omega_c\ /\ \omega_P$ which corresponds to 0.17 nT. The two curves (b) and (d) are slices at z = 100 km and 200 km, respectively, at t = 10 ms.

and the beam pinches only at the edge. In contrast, cold beams with a radius of a few λ_E are noncurrent neutralized and exhibit strong pinching.

2.9.2 Relativistic and Mildly Relativistic Beam Propagation in Plasma

Consider a cold plasma of electrons and ions of density $n_p = 1$ cm^{-3}. A beam of electrons of radius $a = 100$ km at density $n_b/n_p = 8\times10^{-4}$ and a risetime of 0.2 ms propagates from the left in a simulation region of dimension 1,000 km × 300 km (Figure 2.17). The beam is mildly-relativistic with $\beta\gamma = 0.2$. For these values the beam current is $I = 200$ A, and since the Alfvén current $I_A = 17\ \beta\gamma$ kA = 2.5 kA, the beam propagates unhindered, electrically neutralized by the plasma ions (Figure 2.17a).

If the beam current is increased to $I = 6.4$ kA ($n_b/n_p = 0.1$), it exceeds I_A and no longer propagates as a beam by time $t = 6.6$ ms (Figure 2.17b).

If the beam is relativistic with $\gamma = 2$ and $n_b/n_p = 0.003$, $I = 2.6$ kA and $I_A = 34$ kA. The beam propagates as shown in Figure 2.17c. A slight pinching of the beam front is seen as the current builds up during risetime and before any return current neutralization can be established.

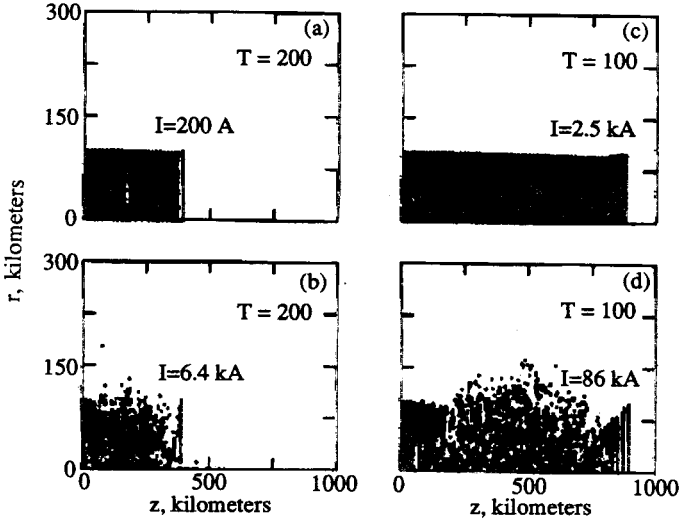

Figure 2.17. Electron beam propagating through a plasma background. The "comb" structure in the incoming beam is an artifact of every 24th particle being plotted.

If the beam current is increased to $I = 86$ kA ($n_b/n_p = 0.1$), it rapidly pinches, converting axial momentum into radial momentum (Figure 2.17d). Some of the kinetic energy of the beam electrons (Figure 2.18a) is transferred to the plasma electrons, causing the background to be heated. Some of the initially cold plasma electrons attain energies as high as 1.5 MeV (Figure 2.18b).

2.9.3 Propagation of a Relativistic Beam Bunch Through Plasma

Consider a cold plasma of electrons and ions of density $n_p = 0.28$ cm^{-3}. A pulse or bunch of $\gamma = 40$ electrons of radius $a = 20$ km, length $l = 8$ km, and density $n_b/n_p = 0.02$ propagates from the left to right, as shown at time $t = 0.5$ ms in Figure 2.19.

The beam pulse produces a "wake field" condition [Keinigs and Jones 1987]: The production of negative and positive plasma electron momenta with a concomitant alternating electric field in the wake of the pulse. The peak strength of the induced fields E_z and E_r are 60 and 20 V/m, respectively. The frequency spectrum of the wake field is sharply peaked at the plasma frequency (4.8 kHz), as is also the case for much longer beam lengths.

2.9.4 Beam Filamentation

Large radius beams ($a >> \lambda_E$) propagating through plasma are susceptible to a filamentation instability [Molvig, Benford, and Condit 1978, Shannahan 1981, Lee and Thode 1983]. The filamentation instability most readily occurs for large currents. In addition, relativistic beams are more susceptible to this instability since the time to filamentation scales as $\gamma^{1/2}$ [Molvig 1975].

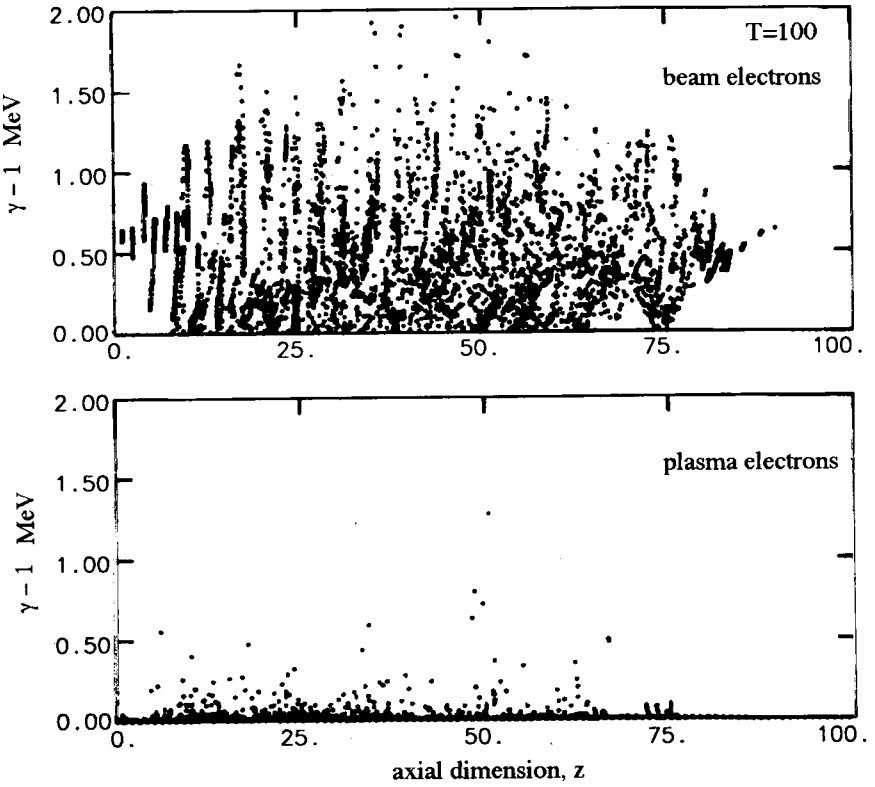

Figure 2.18. (top) Kinetic energy of beam electrons at $t = 100\ \omega_p^{-1}$. (bottom) Kinetic energy of plasma electrons at $t = 100\ \omega_p^{-1}$.

Consider a relativistic beam ($\gamma = 20$) of radius $a = 20\ \lambda_E$ and $n_b/n_p = 0.2$. For this case, the beam current is approximately the same as the Alfvén current (340 kA) so that filamentation is expected.

Figure 2.20 shows the evolution of the beam. As predicted, initially the pinching occurs only near the beam edge. At later time the beam undergoes a strong filamentation instability. The solid beam therefore pinches into current carrying filaments whose thicknesses are of the order of λ_E. The actual width is determined by the factors outlined in Eq.(2.23).

Strong magnetic fields can inhibit beam filamentation, however in most cosmic plasmas $\omega_b \leq \omega_p$ so that filamentation is expected.

2.9.5 Dynamical Evolution of a Narrow Birkeland Filament

Consider a columnar plasma filament with a Gaussian radial density profile [Nielsen, Green, and Buneman 1979]. A large external magnetic field $\beta_p \approx 0.1$ Eq.(8.20) is applied uniformly throughout the plasma column and the simulation region with the field lines parallel to the axis

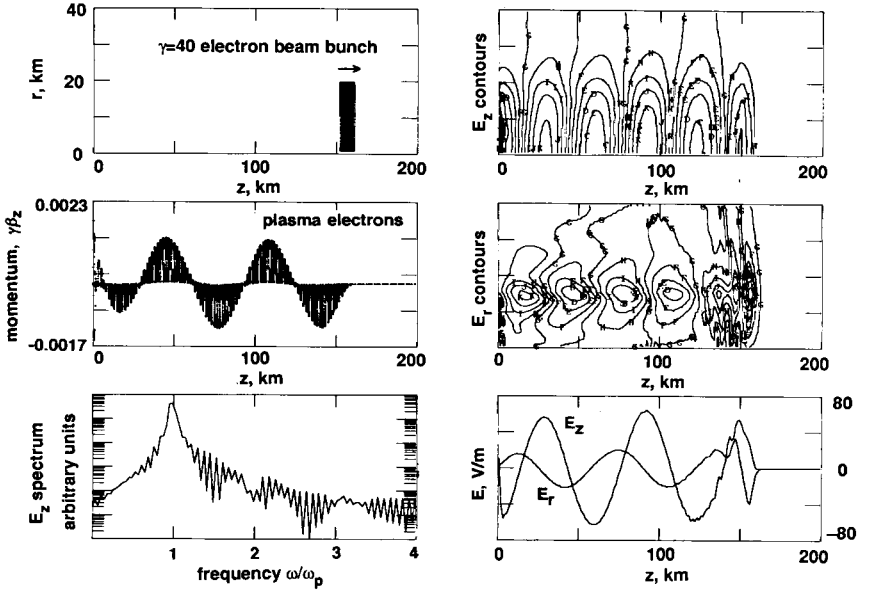

Figure 2.19. Particle, field, and frequency data for a pulsed beam propagating in a plasma.

of the column. Additionally, a strong uniform electric field is applied along the column so that significant currents are generated ($B_0/B^{\text{self}} \approx 4.5$). The simulation is periodic in space so that a particle which moves out of one side of the simulation domain is returned at the opposite side with its same velocity. Computer economy forces a time compression by setting $m_i / m_e = 16$ (Section 8.6.3). The number of superparticles per Debye cube is $n \lambda_D^3 \approx 5.4$. This problem was simulated with the 3D code SPLASH (Chapter 8).

After an initial current buildup, accompanied by visible pinching, a sudden a dramatic helical mode developed (Figure 2.21). At this point the ratio of externally applied magnetic field to self-generated magnetic field was about 2.5:1. The effect of the instability was a transport of plasma across B, resulting in a column of radius somewhat larger than the original radius. The magnetostatic energy W_B reaches its peak at $t = 160\ \omega_p^{-1}$ (Figure 2.22a). The onset of the instability converts this into electrostatic energy W_E (Figure 2.22b). The peak of W_E occurs at $t = 184\ \omega_p^{-1}$. This energy is subsequently radiated away (Figure 2.22c,d) as electromagnetic waves. The frequency of radiation is the bulk rotation frequency which for this simulation is less than ω_t. Since there are still relatively few Debye lengths across the column ($a / \lambda_D \approx 12$), it is probable that the entire column, not just the surface, participates in a synchrotron radiation process.

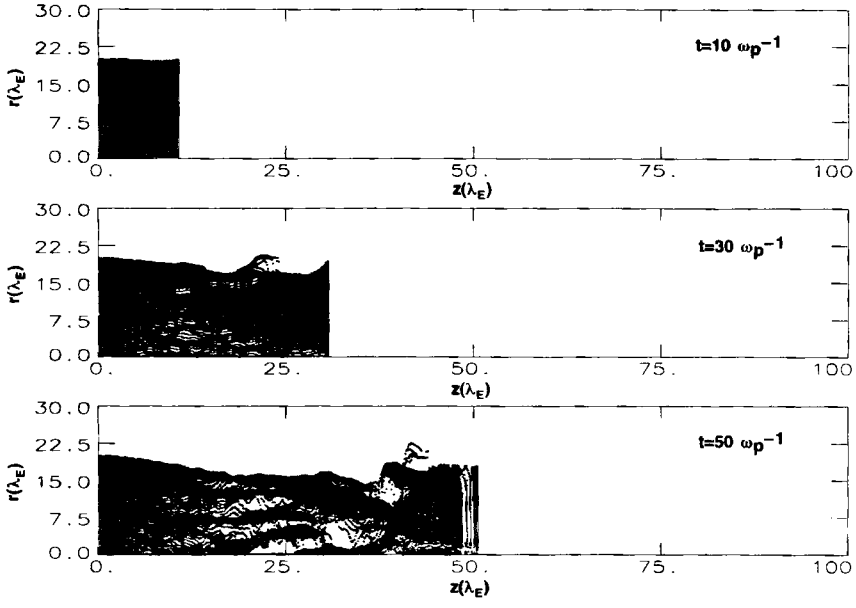

Figure 2.20. Filamentation of a thick (20 λ_E), relativisitic ($\gamma = 20$), current neutralized beam in a plasma.

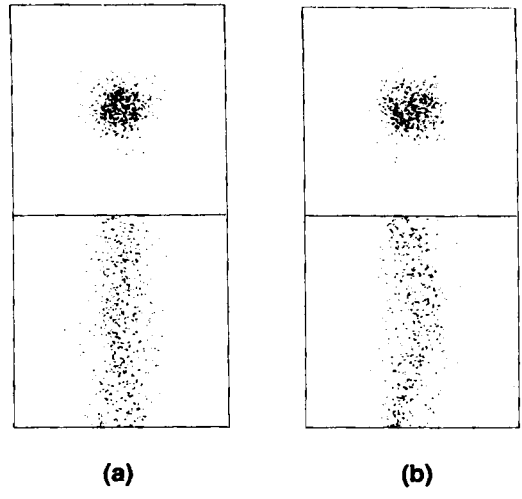

Figure 2.21. Cross-sectional and axial views of the electron distributions in the simulated Birkeland filament (5% of the electrons are plotted). **(a)** Before instability, $t = 150\ \omega_p^{-1}$; **(b)** After helix formation, $t = 164\ \omega_p^{-1}$.

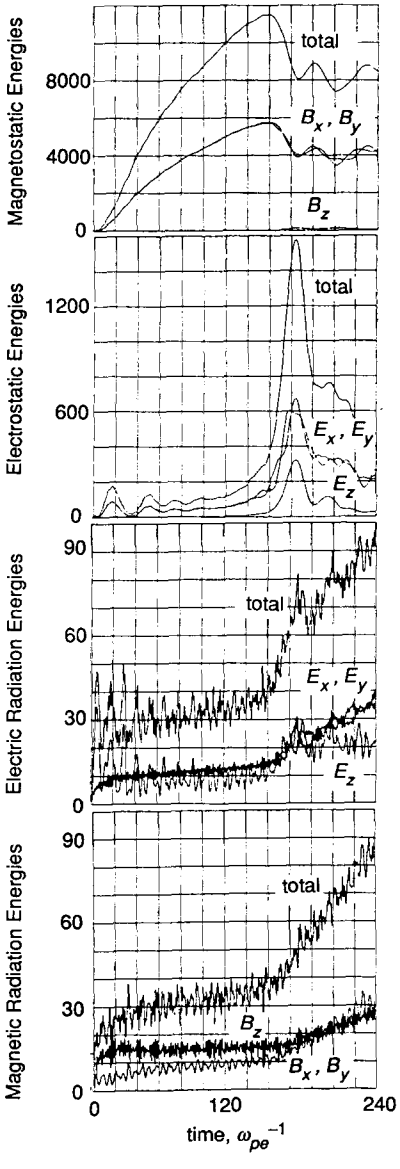

Figure 2.22. Magnetostatic, electrostatic, electric and magnetic radiation energies vs time in ω_p^{-1}. The energies are give in arbitrary energy units.

Figure 2.23. Cross-sectional view of a 2.1 mA electron beam.

2.9.6 Vortex Formation in Thin Cylindrical Electron Beams Propagating Along a Magnetic Field

Historically, vortex structure and vortex interactions in charged particle beams have been known since the turn of the 19th century when Birkeland first photographed the passage of particle beams through low vacuum in his terrella cathode experiments. Cutler (1956), starting with a perfectly circular 2.1 mA electron beam was able to record the vortex structure shown in Figure 2.23 after the beam had propagated for 300 cm along a 34 G field.

The circular beam employed by Cutler was simulated with SPLASH where q=0.04 Eq.(1.15), and $\omega_p dt = 0.25$ [Peratt 1985]. The simulation used 250,000 electrons, 1% of which are plotted in Figure 2.24. This figure shows the time evolution of the diocotron instability over 190 plasma periods and is in good agreement with the measured beam pattern.

The e-folding length for instability buildup is [Kyhl and Webster 1956, Pierce 1956]

$$L = \lambda C B_z V / I \tag{2.94}$$

where C is the beam circumference, B_z is the magnetic field, V is the voltage, and I is the beam current. Figure 2.25 plots the current required to initiate the instability, the formation of simple vortex patterns, and the onset of vortex interactions as a function of the beam length L for a number

Figure 2.24. (Opposite) Cross-sectional views of simulated beam corresponding to the experimental conditions of Figure 2.23 at various time steps. 1% of the electrons are plotted. The vorticity is clockwise for the outwardly directed B_z.

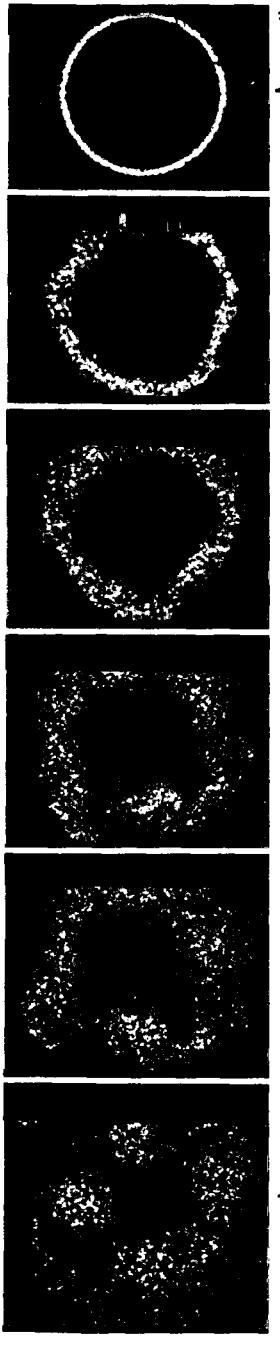
= 0.04
1 ω_p^{-1}
55
75
100
120
190

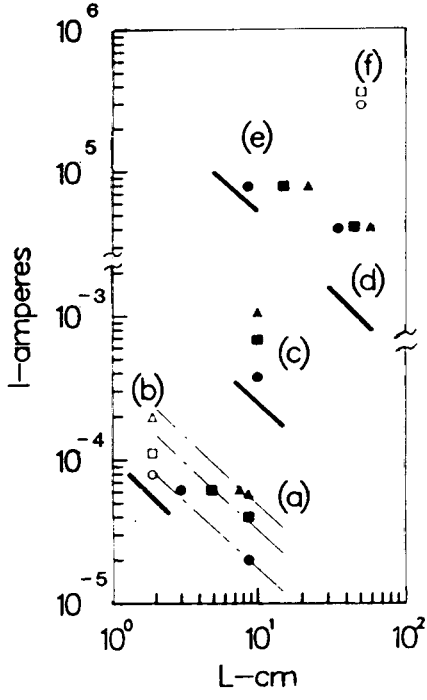

Figure 2.25. Beam current vs distance for instability onset (circles), simple vortex patterns (squares), and vortex interactions (triangles). Experiment (solid symbols), simulation (open symbols), and (2.94) (dark lines). **(a)** $q = 2.5 \times 10^{-3}$, 80 V, $l = 10$; **(b)** $q = 0.04$, 50 V, $l = 4$, $n_i = 0$; **(c)** $q = 7.3 \times 10^{-3}$, 80 V, l=10, $p = 10^{-5}$ T; **(d)** $q = 0.39$, 400 kV, $l = 4$, $p = 0.2$ T; **(e)** $q = 0.59$, 1.9 MV, $l = 10$, $p = 0.3$ T; **(f)** $q = 0.11$, 10 MV, $l = 16$, $n_i = n_e$.

of experimental and simulation cases. Also plotted is the linear-theory prediction for instability onset Eq.(2.94). As shown, the linear theory underestimates the onset by a factor of 2 to 3.

As shown in Figure 2.24, the onset of instability occurs when $\Delta r \approx 10\ \lambda_D$ (after expansion from an initial $2.5\lambda_D$ beam thickness) for a beam of circumference $314\lambda_D$. Thus, the number of vortices expected is $l = C / \lambda \approx 4$, as found in the simulation.

Microwaves from the following radiation mechanism are observed in the simulations. The initially concentric ring contours of the electrostatic field $E_r(r)$ and the induced magnetic field $B_\phi(r)$ form cross-sectional "islands" as the nonlinear state evolves (Figure 2.26, inset). The helical electron flow in a vortex can be generalized into axial and azimuthal current components, thereby producing both long-range attractive and short-range repulsive forces between neighboring vortices (Section 3.10.2), in addition to the electrostatic line-charge repulsive force

$$F \approx + n_e e (1 - f_e) / r \,. \tag{2.95}$$

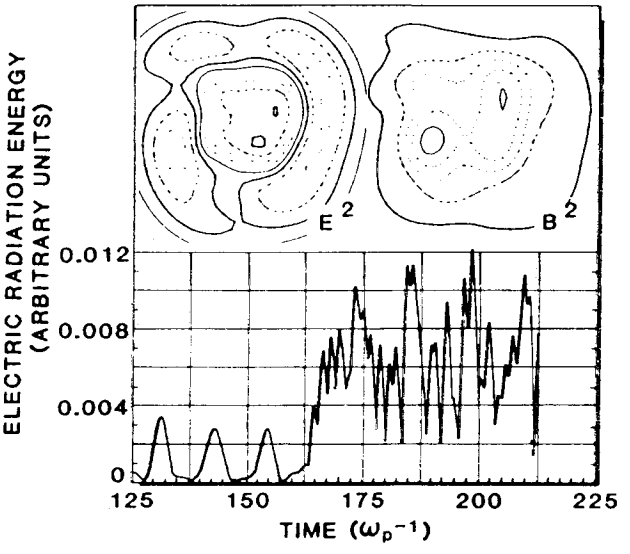

Figure 2.26. Transverse electric field radiation energy vs time in ω_p^{-1}. Inset: Contours of E^2 and B^2 at 175 ω_p^{-1}.

These forces causes the most neighborly filaments to spiral together in coalescence (when $f_e \approx 1$) and also produce microwaves from the rapid changes in the electromagnetic fields during this process (Figure 2.26).

2.9.7 Charge-Neutralized Relativistic Electron Beam Propagation Along a Magnetic Field

Consider the propagation of beam of 7.5 MeV electrons through a plasma of equal numbers of electrons and ions in the presence of an axial magnetic field. To simulate this case, we choose $\omega_p\, dt = 0.25, \lambda_D / \Delta = 0.1, m_i / m_e = 40$, and $T_i / T_e = 1.0$, and an axial magnetic field of strength $\omega_c = 1.0\ \omega_p$. The beam radius is $r_b = 3\ \Delta$ and the beam density is $n_b / \Delta^3 = 3.0$. For 7.5 Mev electrons, $\gamma = 1 + 7.5$ MeV/0.511 MeV = 15.8 and $\beta_z = 0.998$.

For the background plasma we choose $r_p = 5\Delta$ and ion and electron densities $n_i / \Delta^3 = n_e / \Delta^3 = 0.4$. Both the beam and background plasmas are given Gaussian density profiles.

Figure 2.27 shows the end and side views of the beam and plasma evolution versus timestep number. The first frame ($1\ \omega_p^{-1}$) depicts the initial simulation setup. Because the background plasma is tenuous and the beam is thin, the beam is not current neutralized and pinches to a minimum radius $r_b \approx \Delta$ within 25 ω_p^{-1}. Once this "steady state" is reached, small amplitude long wavelength perturbation growth sets in, causing the beam to go unstable. This instability leads to a well-defined helical mode shown in the last frame at 125 ω_p^{-1}.

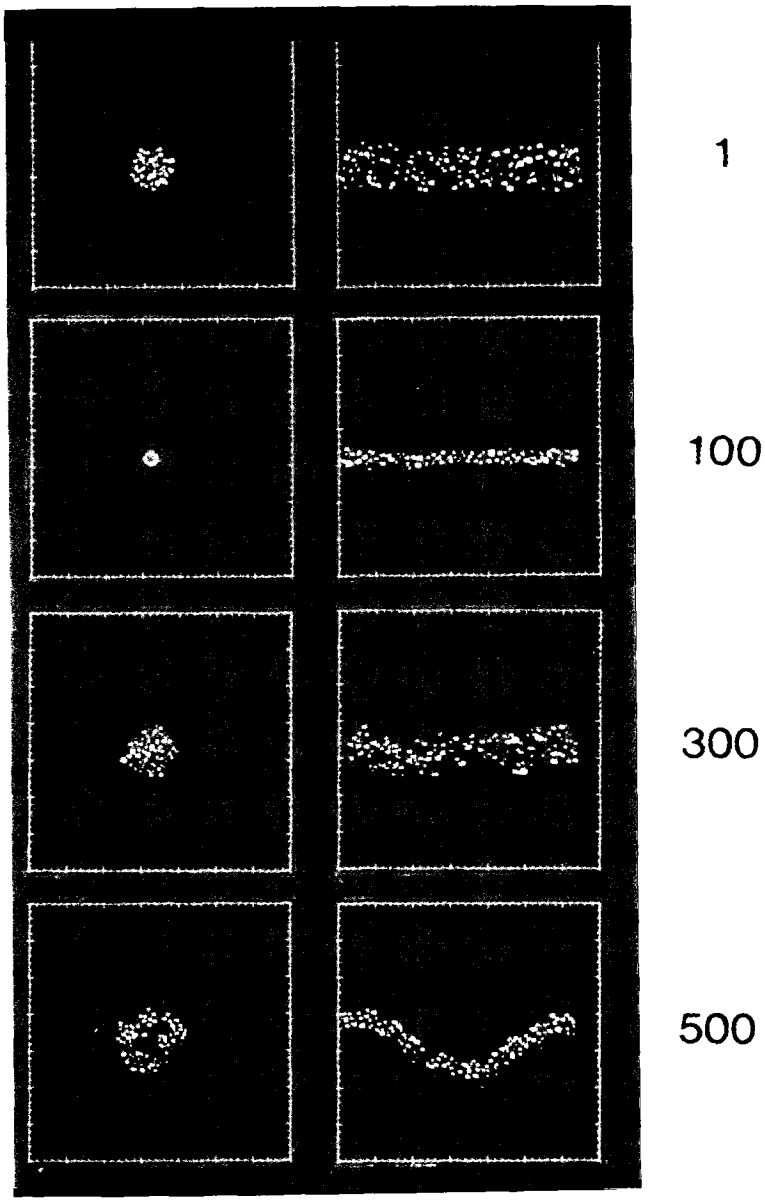

Figure 2.27. Evolution of a non-magnetically neutralized 7.5 MeV electron current in a plasma.

Figure 2.28. Simulated aurora. Current increases continuously from top to bottom in each column. The simulated beam is analogous to the experimental conditions leading to the data shown in Figure 2.15.

2.9.8 Numerical Aurora Simulations

A simulation of the laboratory aurora experiment of Section 2.8.2 is shown in Figure 2.28. The parameters used in this simulation are $q = 0.04$, $\omega_p dt = 0.25$, and $w / \Delta x = 0.1$, where w is the width of the beam. To simulate the continuously increasing voltage applied to the beam, the acceleration parameter E_z / cB_z was set to 0.05. The constant electric field causes the electrons to accelerate in the $-z$ direction and the ions to accelerate in the $+z$ direction, thereby producing a time-increasing beam current, in mimicry of increasing the voltage in the laboratory experiment. The simulated beam patterns shown in Figure 2.28 are to be compared to Figure 2.15. Here we again see an essentially rigid rotor rotation predicted by linear theory until vortices develop on the beam.

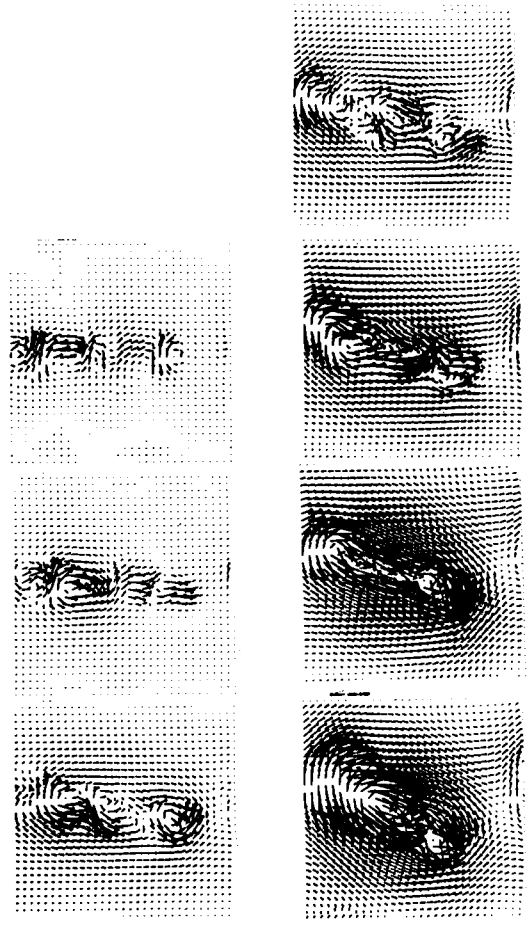

Figure 2.29. "Magnetic storm" produced by self-generated transverse magnetic field during beam vortexing. The length of the arrows indicate relative field strength while direction gives the polarization. These frames coincide with those of Figure 2.28.

The simulation allows an in-depth study of the other beam parameters and Fig 2.29 shows the time evolution of the self-consistent magnetic field produced by the beam. The "magnetic storm" shown corresponds to the beam profiles of Figure 2.28.

Notes

[1] According to Chen (1985): "In a plasma, it is usually possible to assume $n_i = n_e$ and $\nabla \cdot \mathbf{E} \neq 0$ at the same time. We shall call this the *plasma approximation*. It is a fundamental trait of plasmas, one which is difficult for the novice to understand. *Do not use Poisson's equation to obtain* **E** *unless it is unavoidable*!"

[2] This equation differs from the Alfvén-Lawson limiting current, $I_{max} = I_A \beta^2 / [\beta^2 - 1 + f_e]$ because of the differing ways in describing charge neutralization [Witalis 1981].

[3] The dispersion relation for a beam of electrons propagating through a plasma is simply $1 = \omega_p^2/\omega^2 + \omega_b^2/(\omega - kV_b)^2$. If the beam is relativistic ω_b^2 is replaced by ω_b^2/γ^3.

[4] In the prescription for Landau damping [Chen 1984], if the electrons are traveling slower than and in the same direction as the wave, they take energy from it.

[5] The dielectric medium of the Marx bank may be 300,000 liters of transformer oil while the pulseline may contain 400,000 liters of deionized water.

[6] The term "plasmoid" was coined by W. Bostick (1956) to describe the force-free self-magnetic field carrying entities he experimented with.